

# An Energy-Stable Scheme for Incompressible Navier-Stokes Equations with Periodically Updated Coefficient Matrix

Lianlei Lin<sup>1</sup>, Naxian Ni<sup>2</sup>, Zhiguo Yang<sup>2</sup>, Suchuan Dong<sup>2\*</sup>

<sup>1</sup>School of Electronics and Information Engineering  
Harbin Institute of Technology, China

<sup>2</sup>Center for Computational and Applied Mathematics  
Department of Mathematics  
Purdue University, USA

(September 10, 2019)

## Abstract

We present an energy-stable scheme for simulating the incompressible Navier-Stokes equations based on the generalized Positive Auxiliary Variable (gPAV) framework. In the gPAV-reformulated system the original nonlinear term is replaced by a linear term plus a correction term, where the correction term is put under control by an auxiliary variable. The proposed scheme incorporates a pressure-correction type strategy into the gPAV procedure, and it satisfies a discrete energy stability property. The scheme entails the computation of two copies of the velocity and pressure within a time step, by solving an individual de-coupled linear equation for each of these field variables. Upon discretization the pressure linear system involves a constant coefficient matrix that can be pre-computed, while the velocity linear system involves a coefficient matrix that is updated periodically, once every  $k_0$  time steps in the current work, where  $k_0$  is a user-specified integer. The auxiliary variable, being a scalar-valued number, is computed by a well-defined explicit formula, which guarantees the positivity of its computed values. It is observed that the current method can produce accurate simulation results at large (or fairly large) time step sizes for the incompressible Navier-Stokes equations. The impact of the periodic coefficient-matrix update on the overall cost of the method is observed to be small in typical numerical simulations. Several flow problems have been simulated to demonstrate the accuracy and performance of the method developed herein.

Keywords: *energy stability; Navier-Stokes equations; incompressible flows; auxiliary variable; generalized positive auxiliary variable; pressure correction*

## 1 Introduction

This work concerns the numerical approximation of the incompressible Navier-Stokes equations in an energy-stable fashion. Energy-stable approximations are attractive in that they not only preserve the dissipative nature of the underlying continuous Navier-Stokes system, but more practically can potentially allow the use of larger time steps in computer simulations. This type of schemes are the focus of a number of previous works in the literature; see e.g. [25, 28, 30, 12, 19, 10, 23, 14, 4]. These schemes typically treat the nonlinear term fully implicitly or in a linearized fashion. Upon discretization, they would typically entail the solution of nonlinear algebraic systems within a time step, or when only a linear system needs to be solved, would involve time-dependent coefficient matrices and entail frequent re-computations (every time step) of these coefficient matrices [10]. This is a main drawback of traditional energy-stable schemes. Their computational cost per time step is typically high compared with that of semi-implicit type schemes [6, 29, 17, 15, 3, 31, 22, 13, 8, 24], which, albeit only conditionally stable, are more commonly-used in production simulations.

---

\*Author of correspondence. Email: sdong@purdue.edu

An interesting recent development in this area is [21], which describes a discretely energy-stable scheme employing an auxiliary energy variable in its formulation. The Navier-Stokes equations are reformulated and augmented by a dynamic equation for the auxiliary variable, which is a scalar-valued number rather than a field function. A prominent feature of this scheme lies in the reformulation of the nonlinear term,

$$\frac{R(t)}{\sqrt{E(t)}} \mathbf{u} \cdot \nabla \mathbf{u}, \quad (1)$$

where  $\mathbf{u}$  is the velocity,  $R(t)$  is the auxiliary variable and  $E(t)$  is the shifted total kinetic energy of the system. The numerical scheme proposed in [21] treats the  $\mathbf{u} \cdot \nabla \mathbf{u}$  component in an explicit fashion, but controls this explicit component by an implicit treatment of  $\frac{R(t)}{\sqrt{E(t)}}$ . The scheme is shown to satisfy a discrete energy stability property, which is also demonstrated by numerical experiments. The scheme has an interesting property that makes it computationally attractive and competitive. Within each time step it requires only the solution of linear algebraic systems with constant coefficient matrices, which can be pre-computed, for the field functions. One does need to additionally solve a nonlinear algebraic equation about a scalar-valued number. But since this nonlinear equation is about a scalar number, not a field function, its cost is very low, accounting for about a few percent of the total cost per time step [21]. A further development of this approach is discussed very recently in [20], which presents a method for treating the so-called energy-stable open boundary conditions [9, 8, 11, 7] in an energy-stable fashion on the discrete level.

While the auxiliary-variable approach and the numerical scheme from [21] possess a number of attractive properties, certain aspects of the method are less favorable and leave much to be desired. We list some of the issues here:

- The need for solving a nonlinear algebraic equation for the auxiliary variable is highly undesirable. While its computational cost can be negligible, the nonlinear equation causes two complications. First, the existence and uniqueness of the solution for the auxiliary variable from the discrete scheme becomes unknown. Second, the positivity of the computed values for the auxiliary variable, as is physically required by its definition, is uncertain.
- The numerical scheme of [21] is formulated in a setting where the velocity and the pressure are fully coupled, and the discrete energy stability is proven in this coupled setting. When implementing the scheme, the authors have made a further approximation about the boundary vorticity, which de-couples the pressure/velocity computations in actual simulations. The stability proof, however, does not hold if this further approximation is taken into account.
- It is observed in [21] that the accuracy of the method deteriorates when the time step size becomes large (or fairly large). How to improve the accuracy of the method for large (or fairly large) time step sizes, while simultaneously preserving the favorable properties that keep the computational cost relatively low, is an open issue.
- In the definition of the auxiliary variable, a biased total energy (shifted by an energy constant  $C_0$ ) has been used in [21]. It is observed that the  $C_0$  value seems to have an influence on the accuracy of the simulation results (see the Kovasznay flow test of [21]), which is an undesirable aspect.

The first and the second issues in the above list have been addressed by [20]. In the method presented in [20], the nonlinear algebraic equation has been eliminated, and the auxiliary variable at each time step is given by an explicit formula, which ensures that its computed values are always positive. The method is formulated in a setting in which the pressure and velocity are de-coupled (barring the auxiliary variable) by a velocity-correction strategy. This scheme retains the attractive properties found in [21], such as the discrete energy stability and the need to only solve linear algebraic systems with constant pre-computable coefficient matrices.

The numerical scheme of [20] is able to achieve these important properties, in large part, thanks to the adoption of the generalized Positive Auxiliary Variable (gPAV) approach, which was originally developed in [33] for general dissipative systems. gPAV provides a means to use a general class of functions in defining the auxiliary variable, and a systematic procedure for treating dissipative partial differential equations (PDE). The gPAV procedure endows energy stability to the resultant scheme, and also can ensure the positivity of the

computed values of the generalized auxiliary variable [33]. Compared with related works [21, 35, 34, 26, 32], the gPAV framework provides a more favorable way for treating the auxiliary variables, and it applies to very general dissipative systems.

In the current work we focus on the accuracy issue of the auxiliary-variable method as listed above. We would like to explore the possibility to expand its accuracy range, and aim to achieve accuracy at large (or fairly large) time step sizes, without seriously sacrificing the computational cost for incompressible Navier-Stokes equations. Summarized in this paper is our effort in this respect and a numerical scheme that largely achieves this goal.

In the current paper we present an energy-stable scheme for the incompressible Navier-Stokes equations employing the gPAV strategy. The salient feature of the scheme lies in the reformulation and numerical treatment of the nonlinear term. In the gPAV-reformulated system we replace the nonlinear term by a linear term plus a correction term, and put the correction term under control by an auxiliary variable (a scalar-valued number). Upon discretization, this leads to a velocity linear algebraic system with a coefficient matrix that can be updated periodically, in particular once every  $k_0$  time steps in the current work, where  $k_0$  is a user-specified integer parameter. The proposed scheme is observed to produce accurate results at large or fairly large time step sizes (depending on the Reynolds number). It substantially expands the accuracy range for the time step size compared with the scheme of [21] and the scheme without the current reformulation of the nonlinear term. Incidentally, we observe that this scheme is not sensitive to the energy constant  $C_0$  used in defining the auxiliary variable.

The current scheme incorporates the gPAV idea and a pressure-correction type splitting strategy, and is endowed with several attractive properties. It is energy-stable and satisfies a discrete energy stability property. No nonlinear solver is involved in this scheme, for either the field functions or the auxiliary variable. The computations for the velocity and the pressure are de-coupled. The method requires the computation of two copies of the velocity and pressure within a time step, by solving an individual de-coupled linear equation for each of them. Upon discretization, the pressure linear algebraic system involves a constant coefficient matrix that can be pre-computed, while the velocity linear system involves a coefficient matrix that can be updated periodically (every  $k_0$  time steps). The auxiliary variable is computed by a well-defined explicit formula, which guarantees the positivity of its computed values.

The coefficient-matrix update induces an extra cost, due to the re-computation and factorization involved therein. But since this is performed only occasionally (every  $k_0$  time steps), this extra cost is effectively spread over  $k_0$  time steps. In numerical simulations  $k_0$  can typically range from several dozen to several hundred, depending on the Reynolds number ( $k_0 = 20$  in the majority of simulations reported herein). So the impact of occasional coefficient matrix update on the overall computational cost of the current method is quite small, and can essentially be negligible in many cases.

The contribution of this work lies in the energy-stable scheme for the incompressible Navier-Stokes equations developed herein. Its favorable properties include: (i) improved accuracy, producing accurate simulation results at large (or fairly large) time step sizes; (ii) relatively low computational cost, requiring only the solution of linear systems with coefficient matrices that are pre-computable or only need to be updated periodically; and (iii) low sensitivity to the energy constant  $C_0$ .

The rest of this paper is organized as follows. In Section 2 we discuss the reformulation of the incompressible Navier-Stokes equations based on the gPAV framework, and present the energy-stable scheme for the reformulated system. We prove a discrete energy stability property of the scheme, and discuss the solution algorithm and its implementation based on high-order spectral elements [27, 1, 16, 5]. In Section 3 we test the proposed method using several flow problems and investigate its accuracy, the effect of algorithmic parameters, and the computational cost. Section 4 then concludes the presentation with comments on a number of related issues.

## 2 Energy-Stable Scheme for Incompressible Flows

### 2.1 Governing Equations and gPAV-Reformulated Equivalent System

Consider some flow domain  $\Omega$  (with boundary  $\partial\Omega$ ) in two or three dimensions, and an incompressible flow contained in  $\Omega$ . The dynamics of the system is described by the incompressible Navier-Stokes equations

given by, in non-dimensional form,

$$\frac{\partial \mathbf{u}}{\partial t} + \mathbf{N}(\mathbf{u}) + \nabla p - \nu \nabla^2 \mathbf{u} = \mathbf{f}, \quad (2)$$

$$\nabla \cdot \mathbf{u} = 0, \quad (3)$$

where  $\mathbf{u}(\mathbf{x}, t)$  is the velocity,  $p(\mathbf{x}, t)$  is the pressure, the nonlinear term  $\mathbf{N}(\mathbf{u}) = \mathbf{u} \cdot \nabla \mathbf{u}$ ,  $\mathbf{f}(\mathbf{x}, t)$  is an external body force, and  $\mathbf{x}$  and  $t$  are the spatial coordinate and time.  $\nu$  is the non-dimensional viscosity (inverse of Reynolds number  $Re$ ),

$$\nu = \frac{1}{Re} = \frac{\nu_f}{U_0 L} \quad (4)$$

where  $U_0$  and  $L$  are respectively the characteristic velocity and length scales, and  $\nu_f$  is the kinematic viscosity of the fluid. We assume Dirichlet boundary condition in this work,

$$\mathbf{u}|_{\partial\Omega} = \mathbf{w}(\mathbf{x}, t) \quad (5)$$

where  $\mathbf{w}$  is the boundary velocity. The governing equations are supplemented by the initial condition

$$\mathbf{u}(\mathbf{x}, 0) = \mathbf{u}_{in}(\mathbf{x}) \quad (6)$$

where  $\mathbf{u}_{in}$  is the initial velocity distribution that satisfies equation (3) and is compatible with the boundary velocity  $\mathbf{w}(\mathbf{x}, t)$  on  $\partial\Omega$  at  $t = 0$ . To fix the pressure we will impose the often-used condition

$$\int_{\Omega} p d\Omega = 0. \quad (7)$$

By taking the  $L^2$  inner product between equation (2) and  $\mathbf{u}$ , integrating by part and using equation (3), we obtain the energy balance equation

$$\frac{\partial}{\partial t} \int_{\Omega} \frac{1}{2} |\mathbf{u}|^2 d\Omega = -\nu \int_{\Omega} \|\nabla \mathbf{u}\|^2 d\Omega + \int_{\partial\Omega} \left[ -p \mathbf{n} + \nu \mathbf{n} \cdot \nabla \mathbf{u} - \frac{1}{2} (\mathbf{n} \cdot \mathbf{u}) \mathbf{u} \right] \cdot \mathbf{u} dA, \quad (8)$$

where  $\|\nabla \mathbf{u}\|^2 = \sum_{i,j=1}^{d_{im}} \partial_i u_j \partial_i u_j$  and  $d_{im}$  is the dimension in space.

We define a biased energy,

$$E(t) = E[\mathbf{u}] = \int_{\Omega} \frac{1}{2} |\mathbf{u}|^2 d\Omega + C_0, \quad (9)$$

where  $C_0$  is a chosen energy constant such that  $E(t) > 0$  for all  $t \geq 0$ . Following the gPAV framework from [33] and also the work [21], we introduce an auxiliary variable  $R(t)$  by

$$\begin{cases} E(t) = R^2, \\ R(t) = \sqrt{E(t)}. \end{cases} \quad (10)$$

It is important to note that both  $E(t)$  and  $R(t)$  are scalar-valued numbers, not field functions. Based on its definition,  $R(t)$  satisfies the following evolution equation

$$2R \frac{dR}{dt} = \int_{\Omega} \mathbf{u} \cdot \frac{\partial \mathbf{u}}{\partial t} d\Omega. \quad (11)$$

Noting that  $\frac{R^2(t)}{E(t)} = 1$ , we reformulate equation (2) into an equivalent form

$$\frac{\partial \mathbf{u}}{\partial t} + \mathbf{M}(\mathbf{u}) + \nabla p - \nu \nabla^2 \mathbf{u} + \frac{R^2}{E(t)} [\mathbf{N}(\mathbf{u}) - \mathbf{M}(\mathbf{u})] = \mathbf{f}, \quad (12)$$

where  $\mathbf{M}(\mathbf{u})$  is defined by,

$$\mathbf{M}(\mathbf{u}) = \mathbf{u}_0 \cdot \nabla \mathbf{u} + \frac{1}{2}(\nabla \cdot \mathbf{u}_0)\mathbf{u}, \quad (13)$$

and  $\mathbf{u}_0$  is a prescribed velocity field that is only occasionally updated in time. In the current paper we choose  $\mathbf{u}_0$  to be the velocity field  $\mathbf{u}$  at every  $k_0$ -th time step, where  $k_0$  is an integer parameter provided by the user. More specifically, at any time step  $n$ ,  $\mathbf{u}_0$  is taken to be the velocity field  $\mathbf{u}$  at time step  $mk_0$ , where  $m$  is the integer satisfying  $mk_0 \leq n < (m+1)k_0$ . Therefore,  $\mathbf{u}_0$  is updated only once every  $k_0$  time steps.

We reformulate equation (11) as follows,

$$\begin{aligned} 2R \frac{dR}{dt} &= \int_{\Omega} \mathbf{u} \cdot \frac{\partial \mathbf{u}}{\partial t} d\Omega \\ &+ \left( \frac{R^2}{E} - 1 \right) \int_{\Omega} [-\mathbf{M}(\mathbf{u}) - \nabla P + \nu \nabla^2 \mathbf{u} + \mathbf{f}] \cdot \mathbf{u} d\Omega \\ &+ \frac{R^2}{E} \left[ \int_{\Omega} (\mathbf{N}(\mathbf{u}) - \mathbf{M}(\mathbf{u})) \cdot \mathbf{u} d\Omega - \int_{\Omega} (\mathbf{N}(\mathbf{u}) - \mathbf{M}(\mathbf{u})) \cdot \mathbf{u} d\Omega \right] \\ &+ \left( 1 - \frac{R^2}{E} \right) \left| \int_{\Omega} \mathbf{f} \cdot \mathbf{u} d\Omega \right| + \left( 1 - \frac{R^2}{E} \right) \left| \int_{\partial\Omega} \left[ -P\mathbf{n} + \nu \mathbf{n} \cdot \nabla \mathbf{u} - \frac{1}{2}(\mathbf{n} \cdot \mathbf{u})\mathbf{u} \right] \cdot \mathbf{u} dA \right| \quad (14) \\ &= \int_{\Omega} \mathbf{u} \cdot \frac{\partial \mathbf{u}}{\partial t} d\Omega + \int_{\Omega} \left[ \mathbf{M}(\mathbf{u}) + \nabla P - \nu \nabla^2 \mathbf{u} + \frac{R^2}{E} (\mathbf{N}(\mathbf{u}) - \mathbf{M}(\mathbf{u})) - \mathbf{f} \right] \cdot \mathbf{u} d\Omega \\ &+ \frac{R^2}{E} \left[ - \int_{\Omega} \nabla P \cdot \mathbf{u} d\Omega + \int_{\Omega} \nu \nabla^2 \mathbf{u} \cdot \mathbf{u} d\Omega - \int_{\Omega} \mathbf{N}(\mathbf{u}) \cdot \mathbf{u} d\Omega + \int_{\Omega} \mathbf{f} \cdot \mathbf{u} d\Omega \right] \\ &+ \left( 1 - \frac{R^2}{E} \right) \left| \int_{\Omega} \mathbf{f} \cdot \mathbf{u} d\Omega \right| + \left( 1 - \frac{R^2}{E} \right) \left| \int_{\partial\Omega} \left[ -P\mathbf{n} + \nu \mathbf{n} \cdot \nabla \mathbf{u} - \frac{1}{2}(\mathbf{n} \cdot \mathbf{u})\mathbf{u} \right] \cdot \mathbf{u} dA \right|. \end{aligned}$$

Note that in the above equation a number of zero terms have been incorporated into the right hand side (RHS). In this equation  $P$  is a field function related to the pressure  $p$  (not  $p$  itself), and will be specified later in equation (25). Note that

$$\begin{aligned} - \int_{\Omega} \nabla P \cdot \mathbf{u} d\Omega + \int_{\Omega} \nu \nabla^2 \mathbf{u} \cdot \mathbf{u} d\Omega - \int_{\Omega} \mathbf{N}(\mathbf{u}) \cdot \mathbf{u} d\Omega = \\ - \int_{\Omega} \nu \|\nabla \mathbf{u}\|^2 d\Omega + \int_{\partial\Omega} \left[ -P\mathbf{n} + \nu \mathbf{n} \cdot \nabla \mathbf{u} - \frac{1}{2}(\mathbf{n} \cdot \mathbf{u})\mathbf{u} \right] \cdot \mathbf{u} dA, \end{aligned}$$

where the integration by part, the divergence theorem, and equation (3) have been used. We can then re-write equation (14) into

$$\begin{aligned} 2R \frac{dR}{dt} &= \int_{\Omega} \mathbf{u} \cdot \frac{\partial \mathbf{u}}{\partial t} d\Omega + \int_{\Omega} \left[ \mathbf{M}(\mathbf{u}) + \nabla P - \nu \nabla^2 \mathbf{u} + \frac{R^2}{E} (\mathbf{N}(\mathbf{u}) - \mathbf{M}(\mathbf{u})) - \mathbf{f} \right] \cdot \mathbf{u} d\Omega \\ &+ \frac{R^2}{E} \left[ - \int_{\Omega} \nu \|\nabla \mathbf{u}\|^2 d\Omega + \int_{\Omega} \mathbf{f} \cdot \mathbf{u} d\Omega + \int_{\partial\Omega} \left[ -P\mathbf{n} + \nu \mathbf{n} \cdot \nabla \mathbf{u} - \frac{1}{2}(\mathbf{n} \cdot \mathbf{w})\mathbf{w} \right] \cdot \mathbf{w} dA \right] \quad (15) \\ &+ \left( 1 - \frac{R^2}{E} \right) \left| \int_{\Omega} \mathbf{f} \cdot \mathbf{u} d\Omega \right| + \left( 1 - \frac{R^2}{E} \right) \left| \int_{\partial\Omega} \left[ -P\mathbf{n} + \nu \mathbf{n} \cdot \nabla \mathbf{u} - \frac{1}{2}(\mathbf{n} \cdot \mathbf{w})\mathbf{w} \right] \cdot \mathbf{w} dA \right|. \end{aligned}$$

Note that the boundary condition (5) has been applied in the above equation. This is the reformulated equivalent form of equation (11)

The reformulated equivalent system of governing equations consists of equations (12), (3) and (15), the boundary condition (5), and the initial condition (6) and the following initial condition for  $R(t)$ ,

$$R(0) = \sqrt{\int_{\Omega} \frac{1}{2} |\mathbf{u}_{in}|^2 d\Omega} + C_0. \quad (16)$$

In this system the dynamic variables are  $\mathbf{u}$ ,  $p$  and  $R$ , and they are all coupled together.  $E(t)$  is given by equation (9). Note that in the reformulated system  $R(t)$  is treated as an approximation of  $\sqrt{E(t)}$  and is computed by solving this system of equations, not by using equation (10).

## 2.2 Numerical Scheme and Unconditional Energy Stability

We next present an unconditionally energy-stable scheme for the reformulated system consisting of equations (12), (3) and (15), and the boundary condition (5).

Let  $n \geq 0$  denote the time step index, and  $(\cdot)^n$  denote the variable  $(\cdot)$  at time step  $n$ . Define

$$\mathbf{u}^0 = \tilde{\mathbf{u}}^0 = \mathbf{u}_{in}, \quad R^0 = R(0) \text{ defined in equation (16)}. \quad (17)$$

We compute  $p^0$  by solving equation (2) (together with (7)) at  $t = 0$ , which in weak form is given by

$$\int_{\Omega} \nabla p^0 \cdot \nabla q d\Omega = \int_{\Omega} [\mathbf{f}^0 - \mathbf{N}(\mathbf{u}_{in})] \cdot \nabla q d\Omega - \nu \int_{\partial\Omega} \mathbf{n} \times (\nabla \times \mathbf{u}_{in}) \cdot \nabla q dA - \int_{\partial\Omega} \mathbf{n} \cdot \left. \frac{\partial \mathbf{w}}{\partial t} \right|^0 q dA, \quad \forall q \in H^1(\Omega). \quad (18)$$

Note that since the boundary velocity  $\mathbf{w}(\mathbf{x}, t)$  is known on  $\partial\Omega$ ,  $\left. \frac{\partial \mathbf{w}}{\partial t} \right|^0$  is well-defined in the above equation.

Then given  $(\mathbf{u}^n, \tilde{\mathbf{u}}^n, R^n, p^n)$  we compute  $(\tilde{\mathbf{u}}^{n+1}, \mathbf{u}^{n+1}, p^{n+1}, R^{n+1})$  together with another auxiliary field function  $\phi^{n+1}$  through the following steps:

For  $\tilde{\mathbf{u}}^{n+1}$ :

$$\frac{\frac{3}{2}\tilde{\mathbf{u}}^{n+1} - 2\mathbf{u}^n + \frac{1}{2}\mathbf{u}^{n-1}}{\Delta t} + \mathbf{M}(\tilde{\mathbf{u}}^{n+1}) + \nabla p^n - \nu \nabla^2 \tilde{\mathbf{u}}^{n+1} + \xi [\mathbf{N}(\tilde{\mathbf{u}}^{*,n+1}) - \mathbf{M}(\tilde{\mathbf{u}}^{*,n+1})] = \mathbf{f}^{n+1}; \quad (19a)$$

$$\xi = \frac{(R^{n+3/2})^2}{E[\bar{\mathbf{u}}^{n+3/2}]}; \quad (19b)$$

$$E[\bar{\mathbf{u}}^{n+3/2}] = \int_{\Omega} \frac{1}{2} \left| \bar{\mathbf{u}}^{n+3/2} \right|^2 d\Omega + C_0; \quad (19c)$$

$$\tilde{\mathbf{u}}^{n+1} = \mathbf{w}^{n+1}, \quad \text{on } \partial\Omega; \quad (19d)$$

For  $\phi^{n+1}$ :

$$\phi^{n+1} = \nabla \cdot \tilde{\mathbf{u}}^{n+1}; \quad (20)$$

For  $p^{n+1}$  and  $\mathbf{u}^{n+1}$ :

$$\frac{\frac{3}{2}\mathbf{u}^{n+1} - \frac{3}{2}\tilde{\mathbf{u}}^{n+1}}{\Delta t} + \nabla (p^{n+1} - p^n + \nu \phi^{n+1}) = 0; \quad (21a)$$

$$\nabla \cdot \mathbf{u}^{n+1} = 0; \quad (21b)$$

$$\mathbf{n} \cdot \mathbf{u}^{n+1} = \mathbf{n} \cdot \mathbf{w}^{n+1}, \quad \text{on } \partial\Omega; \quad (21c)$$

$$\int_{\Omega} p^{n+1} d\Omega = 0; \quad (21d)$$

For  $R^{n+1}$ :

$$\begin{aligned} & \left( \frac{3}{2}R^{n+1} + R^n - \frac{1}{2}R^{n-1} \right) \frac{\frac{3}{2}R^{n+1} - 2R^n + \frac{1}{2}R^{n-1}}{\Delta t} = \int_{\Omega} \tilde{\mathbf{u}}^{n+1} \cdot \frac{\frac{3}{2}\mathbf{u}^{n+1} - 2\mathbf{u}^n + \frac{1}{2}\mathbf{u}^{n-1}}{\Delta t} \\ & + \xi \left[ -\nu \int_{\Omega} \|\nabla \tilde{\mathbf{u}}^{n+1}\|^2 d\Omega + \int_{\Omega} \mathbf{f}^{n+1} \cdot \tilde{\mathbf{u}}^{n+1} d\Omega + \int_{\Omega} \left( -\bar{P}^{n+1} \mathbf{n} + \nu \mathbf{n} \cdot \nabla \tilde{\mathbf{u}}^{n+1} - \frac{1}{2}(\mathbf{n} \cdot \mathbf{w}^{n+1}) \mathbf{w}^{n+1} \right) \cdot \mathbf{w}^{n+1} d\Omega \right] \\ & - \int_{\Omega} [-\mathbf{M}(\tilde{\mathbf{u}}^{n+1}) - \nabla P^{n+1} + \nu \nabla^2 \tilde{\mathbf{u}}^{n+1} - \xi (\mathbf{N}(\tilde{\mathbf{u}}^{*,n+1}) - \mathbf{M}(\tilde{\mathbf{u}}^{*,n+1})) + \mathbf{f}^{n+1}] \cdot \tilde{\mathbf{u}}^{n+1} d\Omega \\ & + (1 - \xi) \left[ \left| \int_{\Omega} \mathbf{f}^{n+1} \cdot \tilde{\mathbf{u}}^{n+1} d\Omega \right| + \left| \int_{\Omega} \left( -\bar{P}^{n+1} \mathbf{n} + \nu \mathbf{n} \cdot \nabla \tilde{\mathbf{u}}^{n+1} - \frac{1}{2}(\mathbf{n} \cdot \mathbf{w}^{n+1}) \mathbf{w}^{n+1} \right) \cdot \mathbf{w}^{n+1} d\Omega \right| \right]. \end{aligned} \quad (22)$$

The symbols in the above equations are defined as follows.  $\Delta t$  is the time step size.  $\tilde{\mathbf{u}}^{n+1}$  and  $\mathbf{u}^{n+1}$  are two different approximations of the velocity  $\mathbf{u}$  at step  $(n+1)$ .  $\tilde{\mathbf{u}}^{*,n+1}$  is a 2nd-order explicit approximation of  $\tilde{\mathbf{u}}^{n+1}$ , given by

$$\tilde{\mathbf{u}}^{*,n+1} = 2\tilde{\mathbf{u}}^n - \tilde{\mathbf{u}}^{n-1}. \quad (23)$$

$\bar{\mathbf{u}}^{n+1}$  and  $\bar{\mathbf{u}}^{n+3/2}$  are second-order approximations of  $\mathbf{u}$  at time steps  $(n+1)$  and  $(n+3/2)$  respectively, and are to be specified later in equation (37).  $R^{n+3/2}$  and  $R^{n+1/2}$  are 2nd-order approximations of  $R(t)$  at time steps  $(n+3/2)$  and  $(n+1/2)$ , defined by

$$R^{n+3/2} = \frac{3}{2}R^{n+1} - \frac{1}{2}R^n, \quad R^{n+1/2} = \frac{3}{2}R^n - \frac{1}{2}R^{n-1}. \quad (24)$$

By equation (20) we mean that  $\phi^{n+1}$  is a projection of  $\nabla \cdot \tilde{\mathbf{u}}^{n+1}$  into the  $H^1(\Omega)$  space. In equation (22)  $P^{n+1}$  and  $\bar{P}^{n+1}$  are defined by

$$P^{n+1} = p^{n+1} + \nu\phi^{n+1}, \quad \bar{P}^{n+1} = \bar{p}^{n+1} + \nu\bar{\phi}^{n+1}, \quad (25)$$

where  $\bar{p}^{n+1}$  and  $\bar{\phi}^{n+1}$  are second-order approximations of  $p^{n+1}$  and  $\phi^{n+1}$  to be specified later in equations (48) and (43). In equation (22), note that  $\frac{1}{2}(\frac{3}{2}R^{n+1} + R^n - \frac{1}{2}R^{n-1})$  is a second-order approximation of  $R^{n+1}$ , satisfying the following property,

$$\begin{aligned} & \left( \frac{3}{2}R^{n+1} + R^n - \frac{1}{2}R^{n-1} \right) \left( \frac{3}{2}R^{n+1} - 2R^n + \frac{1}{2}R^{n-1} \right) \\ &= \left( R^{n+3/2} \right)^2 - \left( R^{n+1/2} \right)^2 = \left( \frac{3}{2}R^{n+1} - \frac{1}{2}R^n \right)^2 - \left( \frac{3}{2}R^n - \frac{1}{2}R^{n-1} \right)^2. \end{aligned} \quad (26)$$

Equations (19a)–(21d) are similar to the rotational pressure correction scheme for the incompressible Navier-Stokes equations, except for the  $\mathbf{M}(\tilde{\mathbf{u}}^{n+1})$  term and the term involving  $\xi$ , which couples these equations together with equation (22). Note that all the terms are enforced at the time step  $(n+1)$ , except the term  $\xi$ , which is approximated at time step  $(n+3/2)$  according to equation (19b). This does not affect the overall second-order accuracy, because  $\xi = \frac{(R^{n+3/2})^2}{E[\bar{\mathbf{u}}^{n+3/2}]}$  is a second-order approximation of  $\frac{R^2(t)}{E(t)} = 1$ . Here the key is to realize that  $\frac{R^2(t)}{E(t)} = 1$  for any time  $t$  on the continuum level. This approximation is a key point in the gPAV framework [33].

The scheme represented by equations (19a)–(22) is energy stable due to the following property.

**Theorem 2.1.** *In the absence of the external force ( $\mathbf{f} = 0$ ) and with homogeneous boundary condition ( $\mathbf{w} = 0$ ), the following relation holds with the scheme given by (19a)–(22),*

$$\left| \frac{3}{2}R^{n+1} - \frac{1}{2}R^n \right|^2 - \left| \frac{3}{2}R^n - \frac{1}{2}R^{n-1} \right|^2 = -\frac{(R^{n+3/2})^2}{E[\bar{\mathbf{u}}^{n+3/2}]} \nu \Delta t \int_{\Omega} \|\nabla \bar{\mathbf{u}}^{n+1}\|^2 d\Omega \leq 0. \quad (27)$$

*Proof.* Take the  $L^2$  inner products between equation (19a) and  $\tilde{\mathbf{u}}^{n+1}$ , and between equation (21a) and  $\tilde{\mathbf{u}}^{n+1}$ . Summing up the two resultant equations together with equation (22), we get

$$\frac{(R^{n+3/2})^2 - (R^{n+1/2})^2}{\Delta t} = \xi \left( -\nu \int_{\Omega} \|\nabla \bar{\mathbf{u}}^{n+1}\|^2 d\Omega + A_1 + A_2 \right) + (1 - \xi) (|A_1| + |A_2|), \quad (28)$$

where we have used the relation (26), and

$$\begin{cases} A_1 = \int_{\Omega} \mathbf{f}^{n+1} \cdot \bar{\mathbf{u}}^{n+1} d\Omega, \\ A_2 = \int_{\Omega} \left( -\bar{P}^{n+1} \mathbf{n} + \nu \mathbf{n} \cdot \nabla \bar{\mathbf{u}}^{n+1} - \frac{1}{2}(\mathbf{n} \cdot \mathbf{w}^{n+1}) \mathbf{w}^{n+1} \right) \cdot \mathbf{w}^{n+1} d\Omega. \end{cases} \quad (29)$$

If  $\mathbf{f} = 0$  and  $\mathbf{w} = 0$ , then  $A_1 = A_2 = 0$ , and equation (28) leads to equation (27) in light of (19b) and (24). Noting that  $E[\bar{\mathbf{u}}^{n+3/2}] > 0$ , the inequality in (27) holds.  $\square$

### 2.3 Solution Algorithm and Implementation

While the system of equations (19a)–(22) are coupled with one another, they can be solved in a de-coupled fashion and the scheme can be implemented in an efficient way, thanks to the fact that the auxiliary variable  $R(t)$  is a scalar number, not a field function. We next present such a solution algorithm.

Let

$$\gamma_0 = \frac{3}{2}; \quad \hat{\mathbf{u}} = 2\mathbf{u}^n - \frac{1}{2}\mathbf{u}^{n-1}. \quad (30)$$

We re-write equation (19a) into

$$\frac{\gamma_0}{\Delta t} \tilde{\mathbf{u}}^{n+1} + \mathbf{M}(\tilde{\mathbf{u}}^{n+1}) - \nu \nabla^2 \tilde{\mathbf{u}}^{n+1} = \mathbf{f}^{n+1} + \frac{\hat{\mathbf{u}}}{\Delta t} - \nabla p^n - \xi [\mathbf{N}(\tilde{\mathbf{u}}^{*,n+1}) - \mathbf{M}(\tilde{\mathbf{u}}^{*,n+1})]. \quad (31)$$

Barring the unknown scalar number  $\xi$ , this is a linear equation with respect to  $\tilde{\mathbf{u}}^{n+1}$ . We solve this equation together with the boundary condition (19d) as follows. Define two field functions  $\tilde{\mathbf{u}}_1^{n+1}$  and  $\tilde{\mathbf{u}}_2^{n+1}$  as solutions to the following problems:

$$\frac{\gamma_0}{\Delta t} \tilde{\mathbf{u}}_1^{n+1} + \mathbf{M}(\tilde{\mathbf{u}}_1^{n+1}) - \nu \nabla^2 \tilde{\mathbf{u}}_1^{n+1} = \mathbf{f}^{n+1} + \frac{\hat{\mathbf{u}}}{\Delta t} - \nabla p^n, \quad (32a)$$

$$\tilde{\mathbf{u}}_1^{n+1} = \mathbf{w}^{n+1}, \quad \text{on } \partial\Omega; \quad (32b)$$

$$\frac{\gamma_0}{\Delta t} \tilde{\mathbf{u}}_2^{n+1} + \mathbf{M}(\tilde{\mathbf{u}}_2^{n+1}) - \nu \nabla^2 \tilde{\mathbf{u}}_2^{n+1} = - [\mathbf{N}(\tilde{\mathbf{u}}^{*,n+1}) - \mathbf{M}(\tilde{\mathbf{u}}^{*,n+1})] \quad (33a)$$

$$\tilde{\mathbf{u}}_2^{n+1} = 0, \quad \text{on } \partial\Omega. \quad (33b)$$

Then for given value  $\xi$  the solution to the equations (19a) and (19d) are given by

$$\tilde{\mathbf{u}}^{n+1} = \tilde{\mathbf{u}}_1^{n+1} + \xi \tilde{\mathbf{u}}_2^{n+1}. \quad (34)$$

Let  $H_0^1(\Omega) = \{ v \in H^1(\Omega) : v|_{\partial\Omega} = 0 \}$ . The weak forms for equations (32a) and (33a) are given by

$$\begin{aligned} & \frac{\gamma_0}{\nu \Delta t} \int_{\Omega} \tilde{\mathbf{u}}_1^{n+1} \varphi d\Omega + \int_{\Omega} \nabla \varphi \cdot \nabla \tilde{\mathbf{u}}_1^{n+1} d\Omega + \frac{1}{\nu} \int_{\Omega} \mathbf{M}(\tilde{\mathbf{u}}_1^{n+1}) \varphi d\Omega \\ & = \frac{1}{\nu} \int_{\Omega} \left( \mathbf{f}^{n+1} + \frac{\hat{\mathbf{u}}}{\Delta t} - \nabla p^n \right) \varphi d\Omega, \quad \forall \varphi \in H_0^1(\Omega); \end{aligned} \quad (35)$$

$$\begin{aligned} & \frac{\gamma_0}{\nu \Delta t} \int_{\Omega} \tilde{\mathbf{u}}_2^{n+1} \varphi d\Omega + \int_{\Omega} \nabla \varphi \cdot \nabla \tilde{\mathbf{u}}_2^{n+1} d\Omega + \frac{1}{\nu} \int_{\Omega} \mathbf{M}(\tilde{\mathbf{u}}_2^{n+1}) \varphi d\Omega \\ & = - \frac{1}{\nu} \int_{\Omega} [\mathbf{N}(\tilde{\mathbf{u}}^{*,n+1}) - \mathbf{M}(\tilde{\mathbf{u}}^{*,n+1})] \varphi, \quad \forall \varphi \in H_0^1(\Omega). \end{aligned} \quad (36)$$

These weak forms, together with the boundary conditions (32b) and (33b), can be implemented using high-order spectral elements in a straightforward fashion.

Define

$$\bar{\mathbf{u}}^{n+1} = \tilde{\mathbf{u}}_1^{n+1} + \tilde{\mathbf{u}}_2^{n+1}, \quad \bar{\mathbf{u}}^{n+3/2} = \frac{3}{2}\bar{\mathbf{u}}^{n+1} - \frac{1}{2}\tilde{\mathbf{u}}^n. \quad (37)$$

Note that these are second-order approximations of  $\tilde{\mathbf{u}}^{n+1}$  and  $\tilde{\mathbf{u}}^{n+3/2}$ , respectively.

To solve for  $\phi^{n+1}$  from (20), in light of (34), we define two field variables  $\phi_1^{n+1}$  and  $\phi_2^{n+2}$  by

$$\phi_1^{n+1} = \nabla \cdot \tilde{\mathbf{u}}_1^{n+1}; \quad (38)$$

$$\phi_2^{n+1} = \nabla \cdot \tilde{\mathbf{u}}_2^{n+1}. \quad (39)$$

Then the solution to (20) is given by

$$\phi^{n+1} = \phi_1^{n+1} + \xi \phi_2^{n+1}, \quad (40)$$

where  $\xi$  is still to be determined. The weak forms for equations (38) and (39) are given by

$$\int_{\Omega} \phi_1^{n+1} \varphi d\Omega = \int_{\Omega} \nabla \cdot \tilde{\mathbf{u}}_1^{n+1} \varphi d\Omega, \quad \forall \varphi \in H^1(\Omega); \quad (41)$$

$$\int_{\Omega} \phi_2^{n+1} \varphi d\Omega = \int_{\Omega} \nabla \cdot \tilde{\mathbf{u}}_2^{n+1} \varphi d\Omega, \quad \forall \varphi \in H^1(\Omega). \quad (42)$$

We define  $\bar{\phi}^{n+1}$  in equation (25) as

$$\bar{\phi}^{n+1} = \phi_1^{n+1} + \phi_2^{n+1}. \quad (43)$$

Note that this is a second-order approximation of  $\phi^{n+1}$ .

To solve equations (21a)–(21d) for  $p^{n+1}$  and  $\mathbf{u}^{n+1}$ , we first derive the weak form of the equations. Let  $q \in H^1(\Omega)$  denote a test function. Taking the  $L^2$  inner product between equation (21a) and  $\nabla q$  leads to

$$\int_{\Omega} \nabla p^{n+1} \cdot \nabla q d\Omega = \int_{\Omega} \left( \frac{\gamma_0}{\Delta t} \tilde{\mathbf{u}}^{n+1} + \nabla p^n - \nu \nabla \phi^{n+1} \right) \cdot \nabla q d\Omega - \frac{\gamma_0}{\Delta t} \int_{\partial\Omega} \mathbf{n} \cdot \mathbf{w}^{n+1} q dA, \quad \forall q \in H^1(\Omega), \quad (44)$$

where we have used integration by part and equation (21c). In light of equations (34) and (40), we define two field variables  $p_1^{n+1}$  and  $p_2^{n+1}$  as solutions to the following equations:

$$\int_{\Omega} \nabla p_1^{n+1} \cdot \nabla q d\Omega = \int_{\Omega} \left( \frac{\gamma_0}{\Delta t} \tilde{\mathbf{u}}_1^{n+1} + \nabla p^n - \nu \nabla \phi_1^{n+1} \right) \cdot \nabla q d\Omega - \frac{\gamma_0}{\Delta t} \int_{\partial\Omega} \mathbf{n} \cdot \mathbf{w}^{n+1} q dA, \quad \forall q \in H^1(\Omega); \quad (45a)$$

$$\int_{\Omega} p_1^{n+1} d\Omega = 0; \quad (45b)$$

$$\int_{\Omega} \nabla p_2^{n+1} \cdot \nabla q d\Omega = \int_{\Omega} \left( \frac{\gamma_0}{\Delta t} \tilde{\mathbf{u}}_2^{n+1} - \nu \nabla \phi_2^{n+1} \right) \cdot \nabla q d\Omega, \quad \forall q \in H^1(\Omega); \quad (46a)$$

$$\int_{\Omega} p_2^{n+1} d\Omega = 0. \quad (46b)$$

Then for given  $\xi$  the solution to equations (44) and (21d) is

$$p^{n+1} = p_1^{n+1} + \xi p_2^{n+1}. \quad (47)$$

With  $p_1^{n+1}$  and  $p_2^{n+1}$  given by equations (45a)–(46b), we define  $\bar{p}^{n+1}$  in (25) as

$$\bar{p}^{n+1} = p_1^{n+1} + p_2^{n+1}. \quad (48)$$

Now we are ready to determine the scalar value  $\xi$ . Note that the combination of equations (19a), (21a) and (22) leads to equation (28). In light of (19b), equation (28) yields the following formula for computing  $\xi$ ,

$$\xi = \frac{(R^{n+1/2})^2 + (|A_1| + |A_2|) \Delta t}{E[\bar{\mathbf{u}}^{n+3/2}] + [\nu \int_{\Omega} \|\nabla \bar{\mathbf{u}}^{n+1}\|^2 d\Omega + (|A_1| - A_1) + (|A_2| - A_2)] \Delta t}, \quad (49)$$

where  $R^{n+1/2}$  is given by (24),  $\bar{\mathbf{u}}^{n+1}$  and  $\bar{\mathbf{u}}^{n+3/2}$  are given by (37), and  $A_1$  and  $A_2$  are given by (29). Then  $R^{n+1}$  is computed as follows,

$$\begin{cases} R^{n+3/2} = \sqrt{\xi E[\bar{\mathbf{u}}^{n+3/2}]}, \\ R^{n+1} = \frac{2}{3} R^{n+3/2} + \frac{1}{3} R^n. \end{cases} \quad (50)$$

It can be noted that  $\xi > 0$  and  $R^{n+3/2} > 0$  for all time steps, and also  $R^{n+1} > 0$  for all time steps, if  $R^{n+1/2}|_{n=0} > 0$ , irrespective of the  $\Delta t$  value or the external force  $\mathbf{f}$  and the boundary velocity  $\mathbf{w}$ . The

Appendix A outlines a method for approximating the variables for the first time step, which ensures that  $R^1 > 0$  and  $R^{n+1/2}|_{n=0} > 0$ .

Combining the above discussions, we end up with the solution algorithm listed in Algorithm 1. This algorithm has the following properties: (i) The computations for the velocity and pressure are de-coupled. (ii) Only linear equations need to be solved within a time step. (iii) The resultant linear algebraic systems upon discretization involve quasi-constant coefficient matrices, which can be updated every  $k_0$  time step sizes ( $k_0$  denoting an integer parameter). (iv) The computed values for the auxiliary variable are guaranteed to be positive. (v) Two copies of the field variables (velocity, pressure and  $\nabla \cdot \tilde{\mathbf{u}}^{n+1}$ ) are computed within a time step. (vi) The algorithm satisfies a discrete energy stability property.

**input** :  $(\mathbf{u}^n, \tilde{\mathbf{u}}^n, p^n, R^n)$ , and these variables of previous time steps  
**output**:  $(\mathbf{u}^{n+1}, \tilde{\mathbf{u}}^{n+1}, p^{n+1}, R^{n+1}, \phi^{n+1})$

**begin**

Solve equations (35) for  $\tilde{\mathbf{u}}_1^{n+1}$ ;

Solve equations (36) for  $\tilde{\mathbf{u}}_2^{n+1}$ ;

Solve equation (41) for  $\phi_1^{n+1}$ ;

Solve equation (42) for  $\phi_2^{n+1}$ ;

Solve equations (45a)–(45b) for  $p_1^{n+1}$ ;

Solve equations (46a)–(46b) for  $p_2^{n+1}$ ;

Compute  $\bar{\mathbf{u}}^{n+1}$ ,  $\bar{\mathbf{u}}^{n+3/2}$ ,  $\bar{\phi}^{n+1}$ ,  $\bar{p}^{n+1}$  and  $\bar{P}^{n+1}$  based on equations (37), (43), (48), and (25);

Compute  $A_1$  and  $A_2$  based on equation (29);

Compute  $\xi$  based on equation (49);

Compute  $\tilde{\mathbf{u}}^{n+1}$  based on equation (34);

Compute  $\phi^{n+1}$  based on equation (40);

Compute  $p^{n+1}$  based on equation (47);

Compute  $R^{n+1}$  based on equation (50);

Compute  $\mathbf{u}^{n+1}$  by equation (21a) as follows,

$$\mathbf{u}^{n+1} = \tilde{\mathbf{u}}^{n+1} - \frac{\Delta t}{\gamma_0} \nabla (p^{n+1} - p^n + \nu \phi^{n+1}); \quad (51)$$

**end**

**Algorithm 1:** Solution algorithm within a time step.

Equations (35)–(36), (41)–(42), and (45a)–(46b) for the field functions  $\tilde{\mathbf{u}}_i^{n+1}$ ,  $\phi_i^{n+1}$  and  $p_i^{n+1}$  ( $i = 1, 2$ ) are already in weak forms, and they can be implemented using  $C^0$  type finite elements or spectral elements in a straightforward fashion. In the current work, these equations are discretized in space using  $C^0$  type spectral elements [27, 16]. Upon discretization, the pressure linear algebraic systems have a symmetric coefficient matrix and are solved using the conjugate gradient (CG) linear solver. The coefficient matrix in the velocity linear algebraic systems is non-symmetric (but positive definite) and is solved using the bi-conjugate gradient stabilized (BiCGStab) linear solver.

**Remark 1.** *In equation (12) we can also choose*

$$\mathbf{M}(\mathbf{u}) = 0, \quad (52)$$

*and use the same algorithm represented by equations (19a)–(22). The energy stability property, Theorem 2.1, still holds for this modified algorithm. The advantage of this modification lies in that the resultant linear algebraic systems upon discretization now involve only constant and time-independent coefficient matrices, which can be pre-computed. However, we observe that this modified algorithm is less accurate than the current algorithm when the time step size increases to moderate or fairly large values. This point will be demonstrated by numerical experiments in Section 3.*

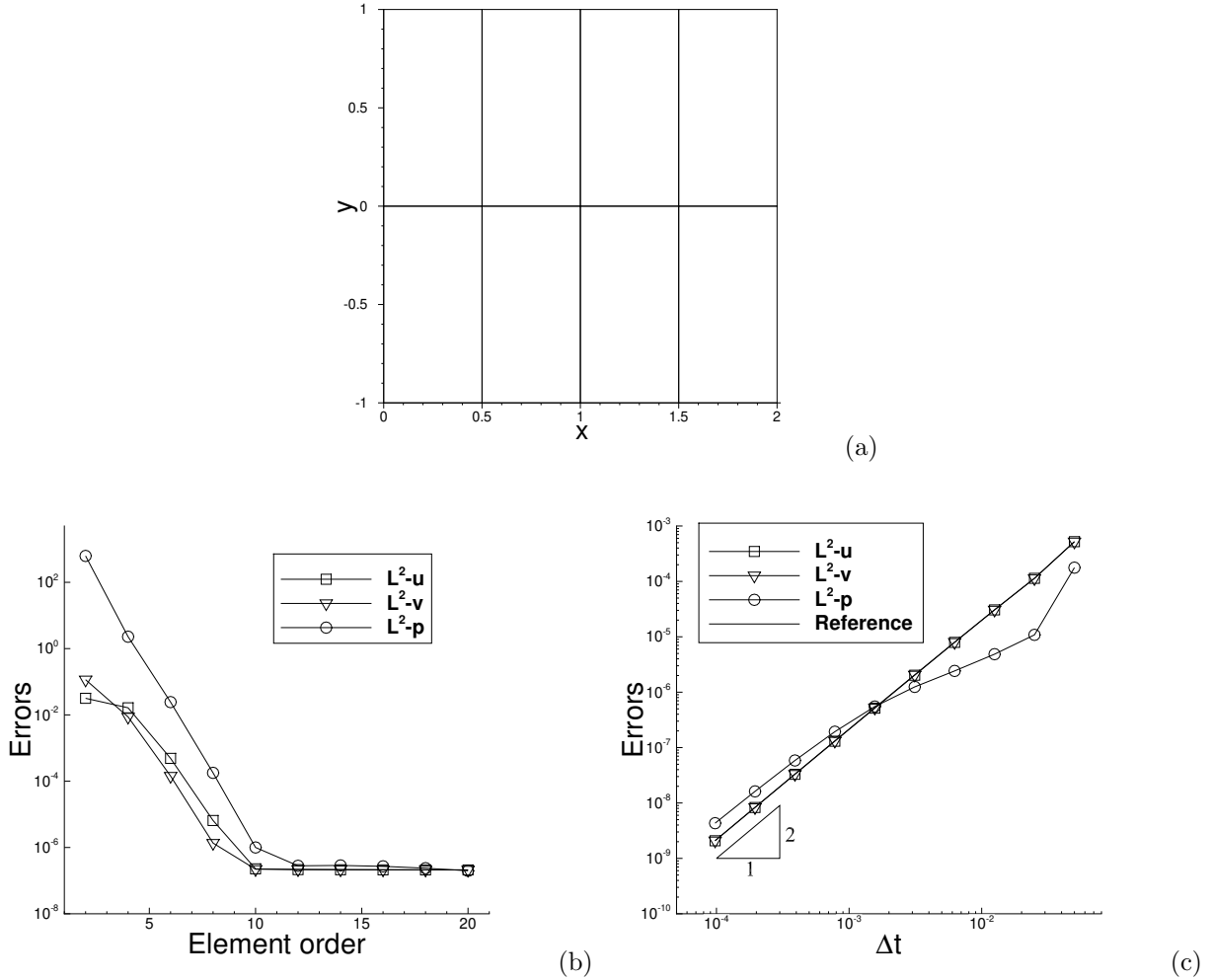


Figure 1: Convergence rates: (a) Computational domain and mesh.  $L^2$  errors of the flow variables as a function of (b) the element order (with fixed  $t_f = 0.1$  and  $\Delta t = 0.001$ ), and (c) the time step size  $\Delta t$  (with fixed  $t_f = 0.1$  and element order 14).

### 3 Representative Numerical Tests

We next use several flow problems in two dimensions to test the performance of the method developed in the previous section. The spatial/temporal convergence rates of the method are first investigated using a manufactured analytic solution. Then the Kovasznay flow and the flow past a hemisphere in a narrow periodic channel are simulated to study the accuracy and stability of the method at large (or fairly large) time step sizes.

#### 3.1 Convergence Rates

We first demonstrate the spatial and temporal convergence rates of the method developed herein using a manufactured analytic solution to the incompressible Navier-Stokes equations. Consider the rectangular domain shown in Figure 1(a),  $0 \leq x \leq 2$  and  $-1 \leq y \leq 1$ , and the following analytic expressions for the flow

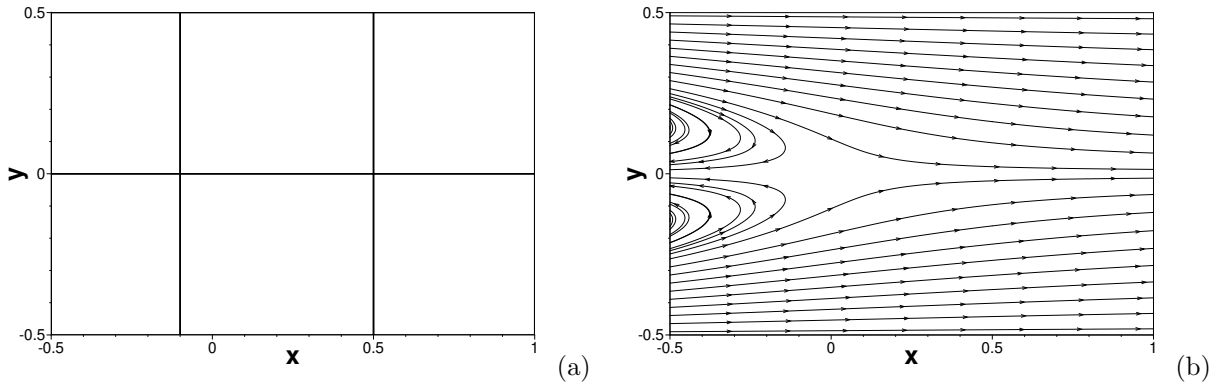


Figure 2: Kovasznay flow: (a) mesh of 6 quadrilateral elements, and (b) flow patterns visualized by streamlines.

variables on this domain,

$$\begin{cases} u = 2 \sin(\pi x) \cos(\pi y) \sin t, \\ v = -2 \cos(\pi x) \sin(\pi y) \sin t, \\ p = 2 \sin(\pi x) \sin(\pi y) \cos t, \end{cases} \quad (53)$$

where  $(u, v)$  are the  $x$  and  $y$  components of the velocity  $\mathbf{u}$ , respectively. In equation (2) the external body force  $\mathbf{f}$  is chosen such that this equation is satisfied by the analytic expressions given in (53). It can be verified that these expressions also satisfy the equation (3).

We discretize the domain using a mesh of 8 quadrilateral elements as shown in Figure 1(a), with 4 elements along the  $x$  direction and 2 along the  $y$  direction. The scheme from Section 2 is employed to solve the incompressible Navier-Stokes equations (2)–(3). Dirichlet boundary condition (5) is imposed on all boundaries, in which the boundary velocity  $\mathbf{w}$  is chosen according to the analytical expressions given in (53). The initial velocity  $\mathbf{u}_{in}$  is obtained by setting  $t = 0$  in the expressions of (53). We employ a fixed  $C_0 = 1000$  in the tests of this subsection. The field  $\mathbf{u}_0$  in  $\mathbf{M}(\mathbf{u})$  (see equation (13)) is updated every 20 time steps ( $k_0 = 20$ ).

We integrate the Navier-Stokes equations from  $t = 0$  to  $t = t_f$  ( $t_f$  to be specified below), and compare the numerical solution at  $t = t_f$  against the analytical solution given by (53). The  $L^2$  norms of the errors for different flow variables have been computed. The element order and the time step size  $\Delta t$  are varied in the spatial and temporal convergence tests, in order to study their effects on the errors of the numerical solutions.

Figure 1(b) illustrates the spatial convergence behavior of the method. Here we use a fixed  $t_f = 0.1$  and time step size  $\Delta t = 0.001$ , and then vary the element order systematically between 2 and 20. This figure shows the  $L^2$  errors of different variables corresponding to these element orders. A clear exponential convergence rate can be observed for element orders below 10. The error curves are observed to level off for element orders above 10, due to the saturation of the temporal truncation errors.

Figure 1(c) is an illustration of the temporal convergence behavior of the method. Here the integration time is fixed at  $t_f = 0.1$  and the element order is fixed at 14. We vary the time step size systematically between  $\Delta t = 0.05$  and  $\Delta t = 9.765625e - 5$ , and plot the  $L^2$  errors of the flow variables as a function of  $\Delta t$ . The temporal convergence rate for the velocity is clearly second-order. It is also observed to be second-order for the pressure when  $\Delta t$  is small. But the pressure convergence behavior is not as uniform as the velocity.

## 3.2 Kovasznay Flow

In this subsection we employ the Kovasznay flow, a steady-state problem with a known analytic solution, to test the accuracy and stability of the current method. This problem has been studied in a number of previous works (see e.g. [2, 16, 10], among others).

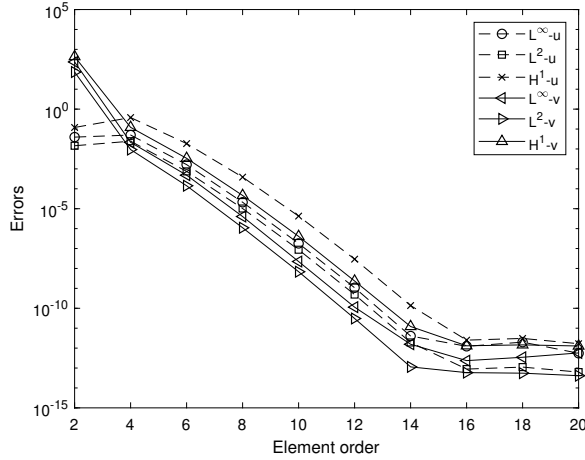


Figure 3: Kovaszny flow: Numerical errors of the steady-state velocity versus the element order.

Consider the domain,  $0.5 \leq x \leq 1$  and  $-0.5 \leq y \leq 0.5$ , as shown in Figure 2(a). The Kovaszny flow is given by the following expressions for the flow variables [18],

$$\begin{cases} u = 1 - \exp(\lambda x) \cos(2\pi y) \\ v = \frac{\lambda}{2\pi} \exp(\lambda x) \sin(2\pi y) \\ p = \frac{1}{2}(1 - \exp(2\lambda x)) \end{cases} \quad (54)$$

with the constant  $\lambda = \frac{1}{2\nu} (1 - \sqrt{1 + 16\pi^2\nu^2})$ . These expressions satisfy the Navier-Stokes equations (2)–(3) with  $\mathbf{f} = 0$ . Figure 2(b) is a visualization of the flow patterns based on the streamlines. We employ a fixed  $\nu = \frac{1}{40}$  in this test.

We employ the method presented in Section 2 to simulate the Kovaszny flow. The flow domain is first discretized using a mesh of 6 quadrilateral spectral elements, as given in Figure 2(a). The element order is varied in the tests, which will be specified below. The external body force in the Navier-Stokes equation (2) is set to  $\mathbf{f} = 0$ . Dirichlet boundary condition (5) is imposed on all domain boundaries, with the boundary velocity  $\mathbf{w}$  chosen according to the analytical expressions from (54). Zero initial velocity ( $\mathbf{u}_{in} = 0$  in (6)) has been employed in all the tests below. The governing equations are integrated to a sufficiently long time so that the flow has reached the steady state. The steady-state solutions are then compared with the analytical expressions from (54) to compute their errors in different norms. The simulation parameter values are varied to investigate their effects on the results, which will be specified in the discussions below.

We vary the element order systematically and have computed the errors of the steady-state solution against the analytic solution in (54) corresponding to different element orders. Figure 3 shows the numerical errors of the steady-state velocity in  $L^\infty$ ,  $L^2$  and  $H^1$  norms as a function of the element order. These results are computed with  $C_0 = 1000$  and  $\Delta t = 0.001$ , and the field  $\mathbf{u}_0$  (and hence the coefficient matrix) is updated every 20 time steps ( $k_0 = 20$ ). The numerical errors decrease exponentially with increasing element order for orders below 14, and the errors saturate at a level around  $10^{-13}$  with element orders beyond 14.

Figure 4 illustrates the typical convergence behavior of the method for the Kovaszny flow. It shows the time histories of the  $L^\infty$  error of the  $x$  velocity component computed with a time step size  $\Delta t = 0.4$  with two element orders 10 and 16. The field  $\mathbf{u}_0$  is updated every 20 time steps ( $k_0 = 20$ ), and  $C_0 = 1000$  in the simulations. The error decreases over time and eventually reaches a steady-state level, around  $10^{-7}$  with element order 10 and around  $10^{-12}$  with order 16. It can take a quite long time for the simulation to reach the steady state, for instance about  $t = 1.5 \times 10^4$  with the element order 16.

Thanks to the energy stability property (Theorem 2.1), stable simulation results can be obtained using the current method with various time step sizes, ranging from small to very large values. This point is demonstrated by the results in Table 1. This table lists the  $L^\infty$  and  $L^2$  errors of the steady-state velocity ( $x$  component  $u$  and  $y$  component  $v$ ) from current simulations corresponding to various  $\Delta t$  values ranging from

Element order	$\Delta t$	$L^\infty - u$	$L^2 - u$	$L^\infty - v$	$L^2 - v$
10	0.004	1.807e-7	8.712e-8	1.807e-7	8.712e-8
	0.005	1.806e-7	8.707e-8	2.284e-8	6.884e-9
	0.006	1.799e-7	8.683e-8	2.277e-8	6.878e-9
	0.007	1.800e-7	8.685e-8	2.289e-8	6.891e-9
	0.008	1.799e-7	8.681e-8	2.295e-8	6.900e-9
	0.01	1.800e-7	8.683e-8	2.313e-8	6.926e-9
	0.02	1.800e-7	8.683e-8	2.371e-8	7.034e-9
	0.03	1.801e-7	8.687e-8	2.409e-8	7.119e-9
	0.04	1.802e-7	8.689e-8	1.802e-7	8.689e-8
	0.05	1.803e-7	8.690e-8	2.455e-8	7.230e-9
	0.06	1.803e-7	8.691e-8	2.470e-8	7.269e-9
	0.07	1.803e-7	8.691e-8	2.482e-8	7.300e-9
	0.08	1.804e-7	8.692e-8	2.492e-8	7.326e-9
	0.1	1.804e-7	8.692e-8	2.508e-8	7.366e-9
	0.2	1.804e-7	8.694e-8	2.548e-8	7.465e-9
	0.3	1.804e-7	8.694e-8	2.564e-8	7.506e-9
	0.4	1.804e-7	8.694e-8	2.573e-8	7.529e-9
	0.5	2.233e-2	7.558e-3	2.233e-2	7.558e-3
	0.75	2.254e-2	4.468e-3	8.565e-3	1.561e-3
	1.0	4.117e-2	7.967e-3	9.873e-3	2.179e-3
2.0	7.901e-2	1.687e-2	2.680e-2	6.113e-3	
10.0	1.939e-1	4.906e-2	4.124e-2	1.064e-2	
100.0	4.895e-1	1.165e-1	9.866e-2	2.442e-2	
16	0.004	7.154e-13	3.241e-14	7.397e-14	1.620e-14
	0.005	4.681e-13	1.820e-14	5.831e-14	9.803e-15
	0.006	2.809e-13	1.245e-14	1.103e-13	8.323e-15
	0.007	3.720e-13	2.829e-14	1.982e-13	8.572e-15
	0.008	6.074e-13	5.108e-14	1.256e-13	8.638e-15
	0.01	1.198e-12	9.969e-14	4.689e-13	1.281e-14
	0.02	1.249e-12	1.054e-13	1.649e-12	9.735e-14
	0.03	1.879e-12	1.625e-13	5.806e-13	1.501e-14
	0.04	7.096e-13	4.212e-14	2.645e-13	1.725e-14
	0.05	2.174e-12	2.078e-13	5.763e-13	1.710e-14
	0.06	1.084e-12	1.296e-13	2.345e-12	1.666e-13
	0.07	2.303e-12	2.222e-13	6.019e-13	1.819e-14
	0.08	2.301e-12	2.069e-13	6.044e-13	1.776e-14
	0.1	2.151e-12	1.768e-13	6.692e-13	1.772e-14
	0.2	2.425e-12	1.671e-13	5.800e-13	1.853e-14
	0.3	1.985e-12	1.733e-13	4.923e-13	1.827e-14
	0.4	4.238e-12	1.451e-12	8.329e-13	2.231e-13
	0.5	3.287e-2	1.002e-2	6.049e-3	1.504e-3
	0.75	4.682e-2	6.360e-3	1.788e-2	2.714e-3
	1.0	4.653e-2	6.507e-3	1.301e-2	2.322e-3
2.0	7.620e-2	1.329e-2	1.993e-2	3.747e-3	
10.0	2.214e-1	5.381e-2	4.510e-2	1.112e-2	
100.0	4.788e-1	1.100e-1	1.033e-1	2.434e-2	

Table 1: Kovasznay flow: effect of  $\Delta t$  on the accuracy of simulation results.  $C_0 = 1000$  and  $\mathbf{u}_0$  is updated every 20 time steps ( $k_0 = 20$ ) in simulations.

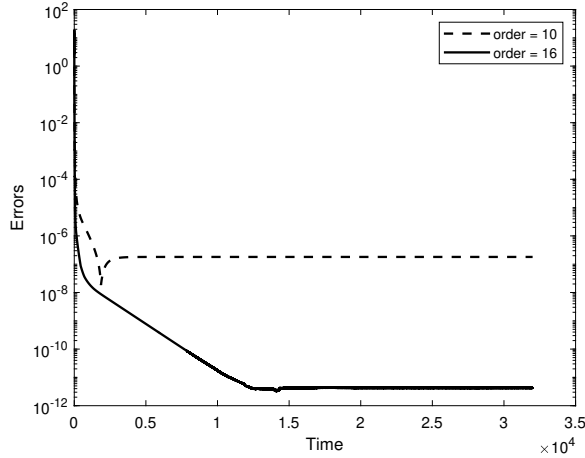


Figure 4: Kovaszny flow: time histories of the  $L^\infty$  error of the  $x$  velocity obtained with two element orders (10 and 16) and a time step size  $\Delta t = 0.4$ .

$C_0$	$L^\infty - u$	$L^2 - u$	$L^\infty - v$	$L^2 - v$
1e-4	1.806e-7	8.709e-8	2.285e-8	6.885e-9
1e-3	1.806e-7	8.709e-8	2.285e-8	6.885e-9
1e-2	1.806e-7	8.709e-8	2.285e-8	6.885e-9
1e-1	1.806e-7	8.709e-8	2.285e-9	6.885e-9
1.0	1.806e-7	8.709e-8	2.285e-8	6.885e-9
10	1.806e-7	8.709e-8	2.285e-8	6.885e-9
100	1.806e-7	8.709e-8	2.285e-8	6.885e-9
1e3	1.806e-7	8.707e-8	2.284e-8	6.884e-9
1e5	1.806e-7	8.706e-8	2.283e-8	6.883e-9
1e7	1.806e-7	8.706e-8	2.283e-8	6.883e-9
1e9	1.806e-7	8.706e-8	2.283e-8	6.883e-9
1e11	1.798e-7	8.678e-8	2.262e-8	6.865e-9
1e12	1.806e-7	8.706e-8	2.283e-8	6.883e-9

Table 2: Kovaszny flow: effect of  $C_0$  on the errors of results.

$\Delta t = 0.004$  to  $\Delta t = 100$ . The results for two element orders, order 10 and order 16, are provided. In these tests  $C_0 = 1000$ , and the coefficient matrix is updated every 20 time steps ( $k_0 = 20$ ). With  $\Delta t = 0.5$  and larger, we observe that the numerical errors fluctuate over time about some level in the long-time simulations. So the errors provided in this table corresponding to such  $\Delta t$  are the time-averaged values. We can make several observations from these results. First, they verify that the current method is indeed stable in long-term simulations, even with large time step sizes. Second, the computation using the current method starts to lose accuracy with time step sizes beyond a certain value, which corresponds to  $\Delta t = 0.5$  and larger for the current problem. Table 1 shows that, for element order 10 the errors for the computed steady-state velocity are at levels  $10^{-9} \sim 10^{-7}$  with time step sizes  $\Delta t \leq 0.4$ , and they increase to a level  $\sim 10^{-2}$  with  $\Delta t \geq 0.5$ . For element order 16 the numerical errors are at a level  $10^{-14} \sim 10^{-12}$  with  $\Delta t \leq 0.4$  and they increase to a level  $\sim 10^{-2}$  with  $\Delta t \geq 0.5$ . It is evident that the current method can produce accurate results at quite large time step sizes. The borderline time step size, beyond which the simulation accuracy starts to deteriorate, is around  $\Delta t = 0.4$  for the Kovaszny flow. This is a very large  $\Delta t$  value for all practical purposes.

When defining the biased energy  $E(t)$  in (9), we need a chosen energy constant  $C_0$  to ensure that  $E(t) > 0$  is satisfied for all time, so that the expression  $\frac{R^2}{E(t)}$  is well-defined in the algorithm. We observe that with the current method the simulation result is not sensitive to the value of  $C_0$ . This is demonstrated by the data in Table 2. Here we have varied  $C_0$  systematically in a range of values between  $10^{-4}$  and  $10^{12}$ , and listed

$\Delta t$	$k_0$	$L^\infty - u$	$L^2 - u$	$L^\infty - v$	$L^2 - v$
0.005	10	3.942e-13	1.728e-14	7.102e-14	8.136e-15
	20	4.681e-13	1.820e-14	5.831e-14	9.803e-15
	50	1.662e-13	1.918e-14	5.122e-14	8.171e-15
	100	4.318e-13	1.860e-14	6.476e-14	9.647e-15
	200	7.341e-13	1.724e-14	6.066e-14	8.516e-15
	500	3.113e-13	1.779e-14	5.350e-14	1.367e-14
	1000	2.643e-13	1.420e-14	5.748e-14	7.974e-15
0.1	10	1.725e-12	1.884e-13	5.914e-13	1.643e-14
	20	2.151e-12	1.768e-13	6.692e-13	1.772e-14
	50	2.185e-12	1.780e-13	6.876e-13	1.735e-14
	100	2.177e-12	1.775e-13	6.913e-13	1.730e-14
	200	2.186e-12	1.773e-13	6.874e-13	1.743e-14
	500	2.191e-12	1.744e-13	6.804e-13	1.730e-14
	1000	2.187e-12	1.732e-13	6.856e-13	1.755e-14

Table 3: Kovaszny flow: effect of the frequency for  $\mathbf{u}_0$  update on simulation errors. Note that  $\mathbf{u}_0$  is updated every  $k_0$  time steps. Element order is 16.

the numerical errors of the steady-state velocity corresponding to these values. These results are computed with an element order 10 and a time step size  $\Delta t = 0.005$ , and the  $\mathbf{u}_0$  field in  $\mathbf{M}(\mathbf{u})$  is updated every 20 time steps ( $k_0 = 20$ ). It is evident that the different  $C_0$  values have little or basically no influence on the numerical errors of the results.

In the current method the field function  $\mathbf{u}_0$  in  $\mathbf{M}(\mathbf{u})$  is updated every  $k_0$  time steps, using a historical velocity field at the time step that is the largest multiple of  $k_0$ , as discussed in Section 2. We observe that for the Kovaszny flow the accuracy of simulation results is not sensitive to the frequency for  $\mathbf{u}_0$  update ( $k_0$  value) in the algorithm. This is demonstrated by Table 3, which lists the errors of the steady-state velocity obtained with various  $k_0$  values ranging from  $k_0 = 10$  to  $k_0 = 1000$  under two time step sizes ( $\Delta t = 0.005$  and 0.1). In this group of tests  $C_0 = 1000$  and the element order is 16. The results are evidently not sensitive to how frequently  $\mathbf{u}_0$  is updated for this problem. The errors are comparable when  $\mathbf{u}_0$  is updated every 1000 time steps or every 10 time steps. The observed insensitivity is due to the fact that the Kovaszny flow eventually reaches a steady state. If the problem is unsteady, very large  $k_0$  values can lead to the deterioration in accuracy of the simulation results, which will be shown in later numerical tests.

In Remark 1 we have suggested a modified algorithm, corresponding to  $\mathbf{M}(\mathbf{u}) = 0$  in the formulation. This modified scheme has a lower computational cost, because the associated velocity coefficient matrix is constant and can be pre-computed. However, it is inferior in accuracy to the current method at moderate and large  $\Delta t$  values, and its accuracy has a strong dependence on the energy constant  $C_0$ . This point is demonstrated by Table 4, which lists the  $L^\infty$  and  $L^2$  errors of the  $x$ -velocity component at steady state obtained using this modified algorithm with various  $\Delta t$  ranging from small to large values. The errors corresponding to two element orders (10 and 16) and several  $C_0$  values are provided. This table can be compared with Table 1, which is obtained using the current method. One can observe that, with the modified algorithm ( $\mathbf{M}(\mathbf{u}) = 0$ ), the simulation loses accuracy with time step sizes  $\Delta t = 0.004$  and larger for element order 10 (and  $\Delta t = 0.002$  and larger for element order 16). The errors reach a level around  $10^{-1}$ . In contrast, with the current method, accurate results can be obtained with time step sizes up to  $\Delta t = 0.4$ ; see Table 1. Table 4 further indicates that with small  $\Delta t$  the accuracy of the modified algorithm ( $\mathbf{M}(\mathbf{u}) = 0$ ) strongly depends on the energy constant  $C_0$ . A larger  $C_0$  leads to considerably more accurate results. This behavior is different from that of the current method, whose accuracy is not sensitive to  $C_0$  as shown by Table 2. A comparison between Table 4 and the data from [21] indicates that this modified algorithm seems also inferior in accuracy to the method of [21]. We note that the modified algorithm here from Remark 1 is based on the pressure-correction type strategy, while the method from [21] is more aligned with a velocity-correction type scheme, which is likely the cause for the observed difference in accuracy.

Element order	$\Delta t$	$C_0 = 10^3$		$C_0 = 10^6$		$C_0 = 10^9$	
		$L^\infty - u$	$L^2 - u$	$L^\infty - u$	$L^2 - u$	$L^\infty - u$	$L^2 - u$
10	0.001	3.201e-3	1.440e-3	3.367e-6	1.517e-6	1.830e-7	8.746e-8
	0.002	4.662e-3	2.097e-3	5.125e-6	2.306e-6	1.837e-7	8.733e-8
	0.003	5.366e-3	2.413e-3	6.151e-6	2.767e-6	1.840e-7	8.724e-8
	0.004	2.580e-1	1.136e-1	4.358e-1	1.836e-1	4.351e-1	1.834e-1
	0.005	2.232e-1	9.872e-2	4.221e-1	1.786e-1	4.332e-1	1.827e-1
	0.006	2.058e-1	9.133e-1	4.268e-1	1.803e-1	4.346e-1	1.832e-1
	0.007	1.967e-1	8.744e-2	4.240e-1	1.793e-1	4.348e-1	1.833e-1
	0.008	6.646e-1	8.564e-2	4.231e-1	1.790e-1	4.331e-1	1.827e-1
	0.01	3.251e-1	1.410e-1	4.356e-1	1.836e-1	4.344e-1	1.831e-1
	0.02	3.938e-1	1.560e-1	4.267e-1	1.803e-1	4.347e-1	1.832e-1
	0.03	3.676e-1	1.488e-1	4.280e-1	1.808e-1	4.355e-1	1.835e-1
	0.04	3.756e-1	1.529e-1	4.347e-1	1.832e-1	4.353e-1	1.835e-1
	0.05	3.827e-1	1.532e-1	4.345e-1	1.832e-1	4.348e-1	1.833e-1
	0.06	4.031e-1	1.548e-1	4.267e-1	1.80e-1	4.352e-1	1.834e-1
	0.07	4.141e-1	1.570e-1	4.339e-1	1.830e-1	4.349e-1	1.833e-1
	0.08	4.218e-1	1.584e-1	4.292e-1	1.812e-1	4.351e-1	1.834e-1
	0.1	4.314e-1	1.604e-1	4.281e-1	1.808e-1	4.352e-1	1.834e-1
	0.2	5.938e-1	1.703e-1	4.309e-1	1.819e-1	4.351e-1	1.834e-1
	0.3	5.937e-1	1.728e-1	4.288e-1	1.811e-1	4.351e-1	1.834e-1
	0.4	4.602e-1	1.690e-1	4.202e-1	1.779e-1	4.348e-1	1.833e-1
0.5	4.752e-1	1.709e-1	4.250e-1	1.797e-1	4.351e-1	1.834e-1	
0.75	5.450e-1	1.777e-1	4.181e-1	1.772e-1	4.356e-1	1.835e-1	
1.0	5.409e-1	1.797e-1	4.166e-1	1.766e-1	4.353e-1	1.835e-1	
2.0	5.487e-1	2.147e-1	4.023e-1	1.712e-1	4.354e-1	1.835e-1	
10.0	5.540e-1	2.113e-1	4.315e-1	1.817e-1	4.357e-1	1.836e-1	
100.0	5.477e-1	2.070e-1	4.326e-1	1.814e-1	4.347e-1	1.833e-1	
16	0.001	3.362e-3	1.513e-3	3.522e-6	1.585e-6	3.513e-9	1.581e-9
	0.002	2.699e-1	1.524e-2	4.293e-1	1.813e-1	4.345e-1	1.832e-1
	0.003	2.853e-1	1.249e-1	4.308e-1	1.818e-1	4.351e-1	1.834e-1
	0.004	2.755e-1	1.207e-1	4.277e-1	1.807e-1	4.349e-1	1.833e-1
	0.005	2.512e-1	1.106e-1	4.304e-1	1.817e-1	4.354e-1	1.835e-1
	0.006	2.305e-1	1.018e-1	4.308e-1	1.818e-1	4.338e-1	1.829e-1
	0.007	2.232e-1	9.873e-2	4.300e-1	1.815e-1	4.350e-1	1.834e-1
	0.008	6.037e-1	1.093e-1	4.264e-1	1.802e-1	4.351e-1	1.834e-1
	0.01	6.084e-1	1.180e-1	4.301e-1	1.816e-1	4.355e-1	1.835e-1
	0.02	3.926e-1	1.358e-1	4.299e-1	1.815e-1	4.354e-1	1.835e-1
	0.03	6.019e-1	1.473e-1	4.261e-1	1.801e-1	4.357e-1	1.836e-1
	0.04	6.038e-1	1.523e-1	4.312e-1	1.820e-1	4.352e-1	1.834e-1
	0.05	6.156e-1	1.558e-1	4.306e-1	1.817e-1	4.350e-1	1.833e-1
	0.06	6.268e-1	1.583e-1	4.297e-1	1.814e-1	4.353e-1	1.834e-1
	0.07	6.185e-1	1.603e-1	4.284e-1	1.809e-1	4.353e-1	1.835e-1
	0.08	6.493e-1	1.620e-1	4.281e-1	1.808e-1	4.354e-1	1.835e-1
	0.1	4.291e-1	1.623e-1	4.296e-1	1.814e-1	4.356e-1	1.836e-1
	0.2	4.392e-1	1.658e-1	4.257e-1	1.800e-1	4.353e-1	1.835e-1
	0.3	4.484e-1	1.674e-1	4.243e-1	1.794e-1	4.352e-1	1.834e-1
	0.4	4.539e-1	1.683e-1	4.238e-1	1.792e-1	4.353e-1	1.835e-1
0.5	4.535e-1	1.689e-1	4.228e-1	1.789e-1	4.352e-1	1.834e-1	
0.75	5.630e-1	1.779e-1	4.191e-1	1.774e-1	4.353e-1	1.835e-1	
1.0	5.527e-1	1.798e-1	4.156e-1	1.761e-1	4.351e-1	1.834e-1	
2.0	5.501e-1	2.147e-1	4.027e-1	1.712e-1	4.354e-1	1.835e-1	
10.0	5.549e-1	2.113e-1	4.174e-1	1.768e-1	4.356e-1	1.836e-1	
100.0	5.480e-1	2.070e-1	4.313e-1	1.801e-1	4.347e-1	1.833e-1	

Table 4: Kovaszny flow: Errors of steady-state velocity obtained using the modified algorithm ( $\mathbf{M}(\mathbf{u}) = 0$ ).

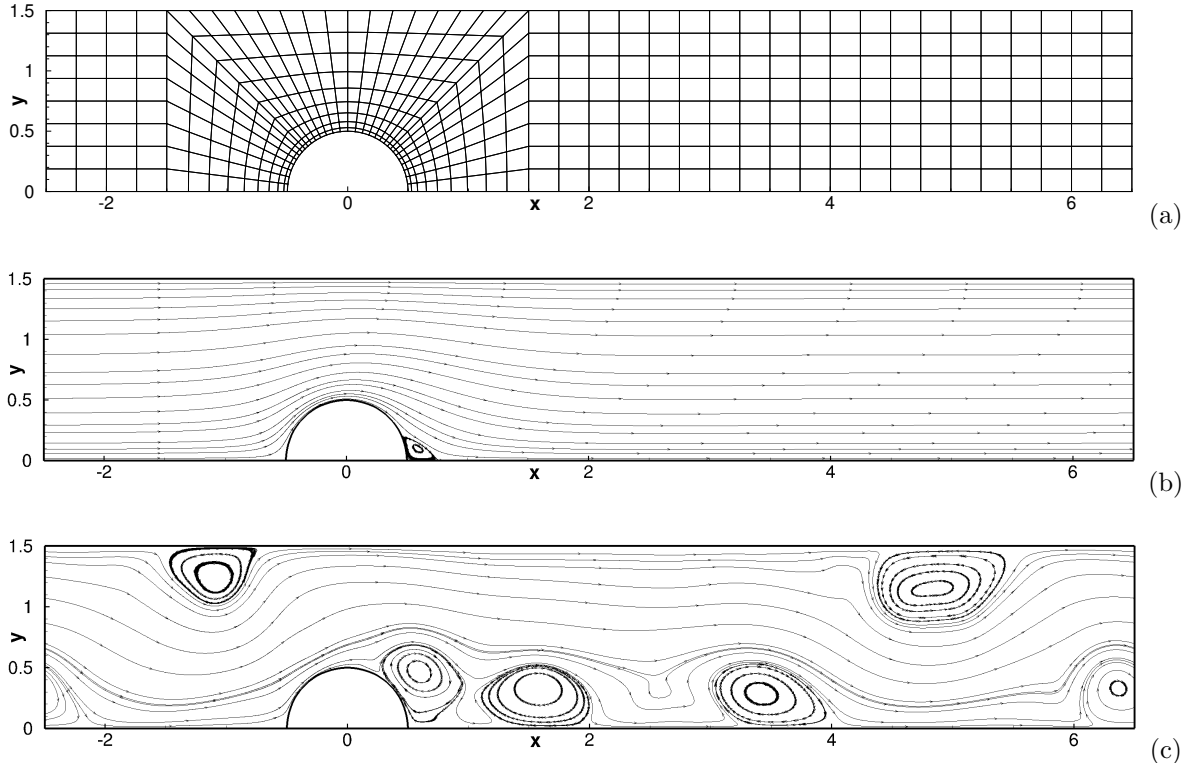


Figure 5: Flow past a hemisphere: (a) flow configuration and a mesh of 480 quadrilateral elements. Flow patterns visualized by streamlines corresponding to  $\nu = 0.02$  (b) and  $\nu = 0.001$  (c).

### 3.3 Flow past a Hemisphere in a Narrow Periodic Channel

In this subsection we test the current method with the flow past a hemisphere in a narrow periodic channel in two dimensions. Specifically, we consider the domain shown in Figure 5(a). A hemisphere (or half-disk) with diameter  $d$  is mounted on the bottom of a narrow channel, which occupies the domain  $-2.5d \leq x \leq 6.5d$  and  $0 \leq y \leq 1.5d$ . The hemispheric center coincides with the origin of the coordinate system. The top and bottom of the channel ( $y = 0, 1.5d$ ) are walls, and in the horizontal direction ( $x = -2.5d, 6.5d$ ) the channel is assumed to be periodic. The flow is driven by a horizontal pressure gradient. This configuration mimics the flow past an infinite array of hemispheres in an infinitely long channel. We choose the hemisphere diameter  $d$  as the length scale and a unit velocity scale  $U_0 = 1$ . All the other physical variables and parameters are then normalized accordingly.

We discretize the domain using a mesh of 480 quadrilateral elements; see Figure 5(a). On the top and bottom channel walls and on the surface of the hemisphere we impose the no-slip condition, i.e. boundary condition (5) with  $\mathbf{w} = 0$ . In the horizontal direction periodic condition is imposed for all the flow variables. The Navier-Stokes equations (2)–(3), with a horizontal body force (pressure gradient) of normalized magnitude  $|\mathbf{f}| = 0.03$ , are solved using the algorithm from Section 2. The element order, the time step size  $\Delta t$ , the energy constant  $C_0$ , the Reynolds number, and other algorithmic parameters are varied to study their effects on the simulation results.

An overview of the characteristics of this flow is provided by Figures 5(b,c), which visualize the flow patterns at two Reynolds numbers corresponding to  $\nu = 0.02$  and  $\nu = 0.001$  using streamlines. At low Reynolds numbers one observes a steady flow (Figure 5(b)). As the Reynolds number increases, vortex shedding can be seen in the hemisphere wake. Due to periodicity, these vortices re-enter the domain from the left, and can interact with the hemisphere and generate complicated dynamics. For instance, vortices can at times be observed near the top channel wall (Figure 5(c)).

We have monitored the total force exerting on the wall surfaces (channel walls and the hemispheric

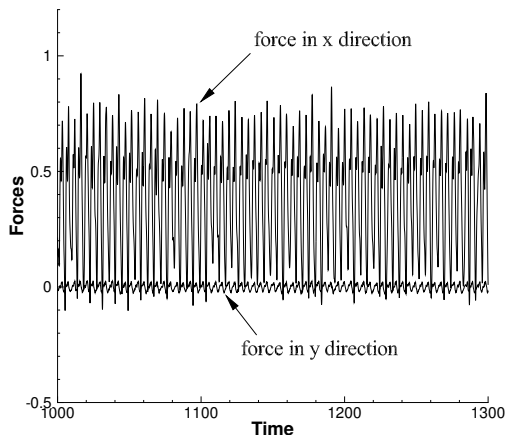


Figure 6: Flow past a hemisphere: Time histories of the forces on the walls with  $\nu = 0.001$ .

surface). Figure 6 shows a typical signal of the force ( $x$  and  $y$  components) at the Reynolds number corresponding to  $\nu = 0.001$ . These are attained using an element order 7,  $\Delta t = 0.001$  and  $C_0 = 1000$  in the simulations. The force signals are fluctuational due to the vortex shedding. The horizontal force (drag) exhibits large fluctuations in magnitude, while the vertical force is much weaker in comparison. The long history and the signal characteristics indicate that the flow has reached a statistically stationary state.

$\nu$	Element order	$f_x$	$f'_x$	$f_y$	$f'_y$	Driving force
0.02	4	0.396	0	7.6e-4	0	0.393
	5	0.394	0	-5.6e-4	0	0.393
	6	0.393	0	8.7e-5	0	0.393
	7	0.393	0	1.4e-5	0	0.393
	8	0.393	0	1.1e-5	0	0.393
0.005	4	0.395	0	-0.192	0	0.393
	5	0.393	0	-4.6e-3	0	0.393
	6	0.393	0	1.6e-2	0	0.393
	7	0.393	0	7.0e-4	0	0.393
	8	0.393	0	-1.3e-4	0	0.393
0.001	4	0.388	0.278	0.129	0.467	0.393
	5	0.405	0.252	-0.0153	0.0443	0.393
	6	0.394	0.238	-0.0636	0.0559	0.393
	7	0.386	0.237	-9.29e-4	0.0134	0.393
	8	0.391	0.241	0.0245	0.0135	0.393
0.0002	4	0.351	0.796	1.353	1.638	0.393
	5	0.437	0.875	0.103	0.276	0.393
	6	0.388	0.812	0.102	0.401	0.393
	7	0.405	0.760	-1.43e-3	0.0829	0.393
	8	0.399	0.725	-0.0865	0.167	0.393

Table 5: Flow past a hemisphere: Effect of spatial resolution on the forces on walls.  $\bar{f}_x$  and  $\bar{f}_y$  are the time-averaged mean forces in  $x$  and  $y$  directions, and  $f'_x$  and  $f'_y$  are the rms forces in the two directions.

From the force histories we can compute the statistical quantities such as the time-averaged mean and root-mean-square (rms) of the forces on the walls. In Table 5 we have listed the mean and rms forces at several Reynolds numbers (for  $\nu$  ranging from  $\nu = 0.02$  to  $\nu = 0.0002$ ), which are computed using element

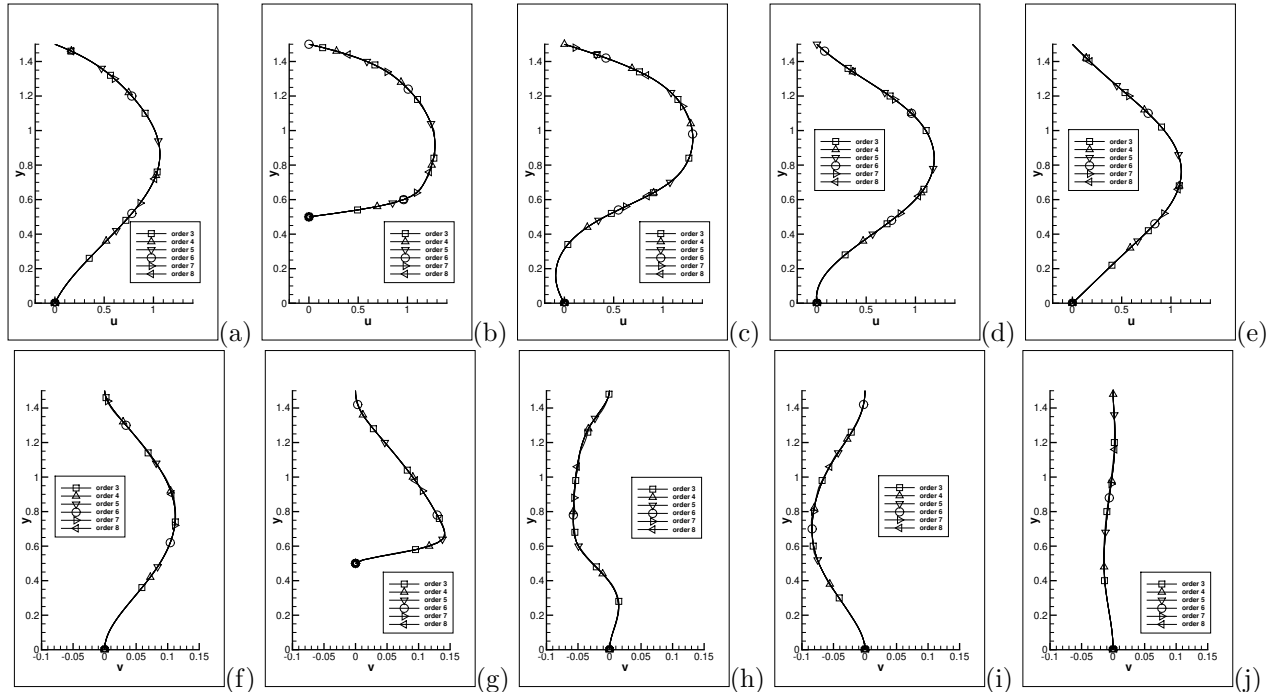


Figure 7: Flow past a hemisphere ( $\nu = 0.005$ ): comparison of profiles of the streamwise velocity  $u$  (top row) and the vertical velocity  $v$  (bottom row) at several downstream locations,  $x/d = -1$  (a, f), 0 (b, g), 1 (c, h), 3 (d, i), 5 (e, j).

orders ranging from 4 to 8. In these simulations fixed values of  $\Delta t = 0.001$  and  $C_0 = 1000$  are employed, and the field  $\mathbf{u}_0$  is updated every 20 time steps ( $k_0 = 20$ ). The total driving force on the domain, i.e. (driving pressure gradient)  $\times$  (domain area)  $= 0.03 \times (1.5 \times 9 - \pi/8) \approx 0.393$ , has also been listed in the table. At a steady state or a statistically stationary state, the time-averaged total horizontal force on the wall should physically match the total driving force in the domain. Therefore, these values can serve as a basic check on the simulation results. At  $\nu = 0.02$  and  $\nu = 0.005$ , it is a steady flow. So given in the table are the steady-state forces, and no time-averaging is performed for these cases. It can be observed that with element orders beyond about 5 the computed values of the horizontal force are quite close to (or for the lower Reynolds numbers the same as) the total driving force on the domain. The rms horizontal force  $f'_x$  also appears to exhibit a sense of convergence with increasing element order. The mean and rms vertical forces ( $\bar{f}_y, f'_y$ ) are quite small when compared with the horizontal counterpart.

Figure 7 shows a comparison of the steady-state streamwise and vertical velocity profiles across the channel at several downstream locations at  $\nu = 0.005$ , computed with various element orders. The velocity profiles corresponding to different element orders essentially overlap with one another. This suggests that these simulations produce essentially the same velocity distribution, and that they have numerically converged with respect to the spatial resolution. The majority of simulation results reported below are computed with an element order 6 or 7.

Figure 8 illustrates the dynamics of the hemisphere flow with a temporal sequence of snapshots of the velocity fields at the Reynolds number corresponding to  $\nu = 0.0005$ . These results are obtained using a time step size  $\Delta t = 0.001$  and  $C_0 = 1000$ , and the field  $\mathbf{u}_0$  is updated every 20 time steps in the simulations. Several effects seem to play a role in the dynamics of this flow: (i) vortex shedding behind the hemisphere; (ii) periodicity of the channel, which introduces vortices into the domain upstream of the hemisphere; (iii) confinement of the narrow channel. The vortices in the hemisphere wake appear to be mostly confined to the regions near the top and bottom walls.

The effect of the energy constant  $C_0$  on the simulation results is studied in Table 6 for the hemisphere flow. This table lists the mean and rms forces on the wall with respect to a range of  $C_0$  values at three Reynolds numbers corresponding to  $\nu = 0.02$ , 0.001 and 0.0002. A time step size  $\Delta t = 0.001$  and element

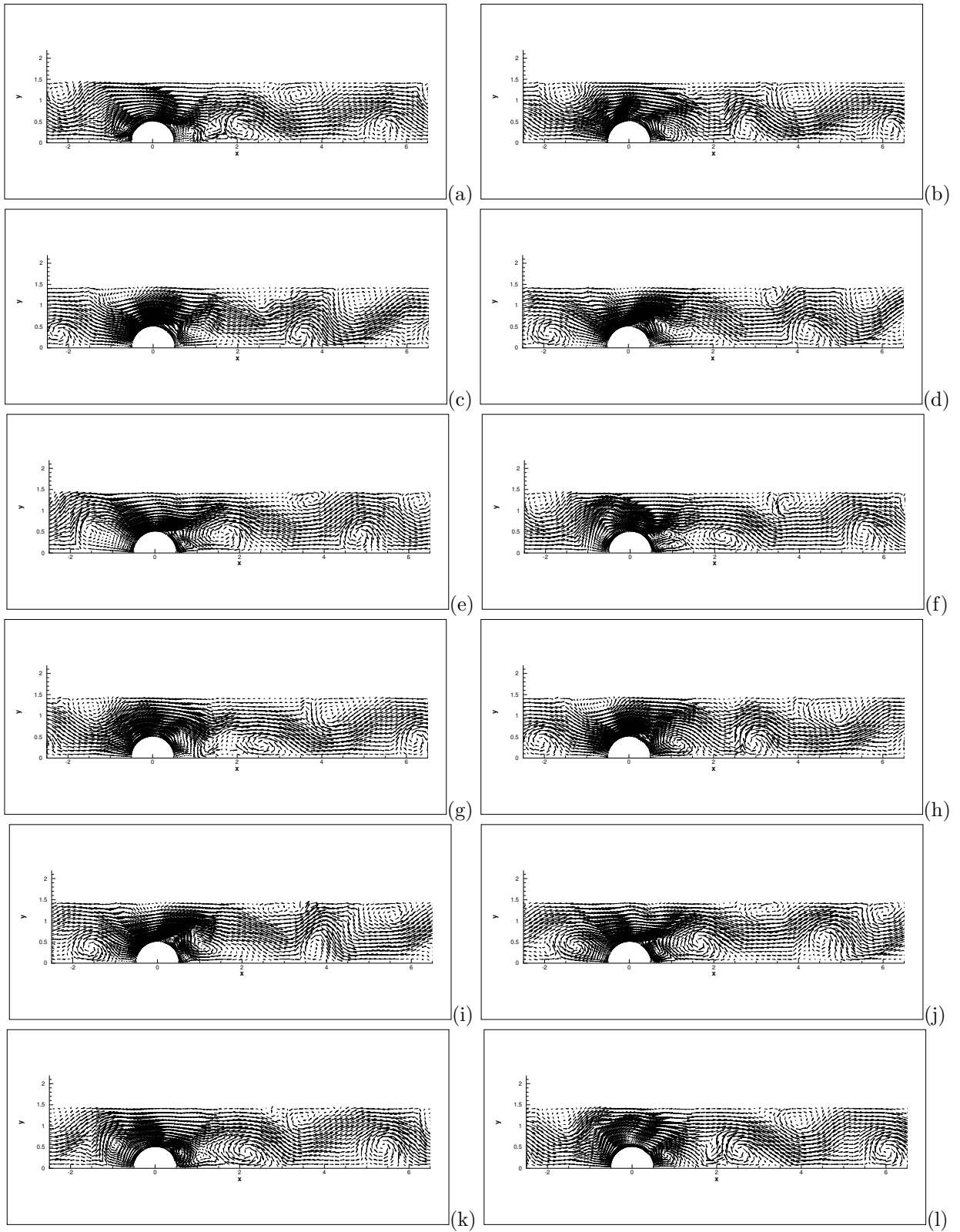


Figure 8: Flow past a hemisphere ( $\nu = 0.0005$ ): temporal sequence of snapshots of the velocity fields at time instants: (a)  $t = t_0$ , (b)  $t = t_0 + 0.8$ , (c)  $t = t_0 + 1.6$ , (d)  $t = t_0 + 2.4$ , (e)  $t = t_0 + 3.2$ , (f)  $t = t_0 + 4.0$ , (g)  $t = t_0 + 4.8$ , (h)  $t = t_0 + 5.6$ , (i)  $t = t_0 + 6.4$ , (j)  $t = t_0 + 7.2$ , (k)  $t = t_0 + 8.0$ , (l)  $t = t_0 + 8.8$ .  $t_0$  denotes the initial time instant. Velocity vectors are plotted on a sparser grid on clarity.

$\nu$	$C_0$	$f_x$	$f'_x$	$f_y$	$f'_y$	Driving force
0.02	1e-2	0.393	0	1.09e-4	0	0.393
	1e0	0.393	0	1.19e-4	0	0.393
	1e+3	0.393	0	8.7e-5	0	0.393
	1e+5	0.393	0	4.3e-5	0	0.393
	1e+7	0.393	0	8.9e-5	0	0.393
0.001	1e-2	0.394	0.242	-0.0696	0.0564	0.393
	1e0	0.394	0.241	-0.0643	0.0563	0.393
	1e+3	0.394	0.238	-0.0636	0.0559	0.393
	1e+5	0.394	0.240	-0.0715	0.0565	0.393
	1e+7	0.394	0.238	-0.0689	0.0558	0.393
0.0002	1e-2	0.386	0.805	0.117	0.408	0.393
	1e0	0.389	0.800	0.0772	0.385	0.393
	1e+3	0.388	0.812	0.102	0.401	0.393
	1e+5	0.388	0.820	0.121	0.421	0.393
	1e+7	0.387	0.825	0.139	0.444	0.393

Table 6: Flow past a hemisphere: Effect of  $C_0$  on the computed forces on the walls.

$\nu$	$\Delta t$	$f_x$	$f'_x$	$f_y$	$f'_y$	Driving force
0.02	0.001	0.393	0	8.7e-5	0	0.393
	0.005	0.393	0	1.05e-4	0	0.393
	0.01	0.393	0	-2.1e-5	0	0.393
	0.1	0.393	0	8.7e-5	0	0.393
	1.0	0.393	0	-2.1e-5	0	0.393
0.001	5e-4	0.393	0.238	-0.0625	0.122	0.393
	0.001	0.394	0.238	-0.0636	0.0559	0.393
	0.005	0.395	0.238	-0.0706	0.0115	0.393
	0.01	0.395	0.216	-0.0681	0.00668	0.393
	0.1	(BiCGStab fails to converge)				
1.0	(BiCGStab fails to converge)					
0.0002	2.5e-4	0.385	0.841	0.172	1.033	0.393
	5e-4	0.387	0.840	0.103	0.784	0.393
	0.001	0.388	0.812	0.102	0.401	0.393
	0.005	0.399	0.671	0.177	0.175	0.393
	0.01	0.393	0.459	-0.00365	0.127	0.393
	0.1	(BiCGStab fails to converge)				
	1.0	(BiCGStab fails to converge)				

Table 7: Flow past a hemisphere: Computed forces on the walls corresponding to a range of  $\Delta t$  values.

order 6 have been employed in this group of tests, and the field  $\mathbf{u}_0$  is updated every 20 time steps. We observe that the obtained forces are essentially the same or quite close corresponding to different  $C_0$ , suggesting that they have a low sensitivity to  $C_0$  using the current method. This is consistent with what has been observed with the Kovaszny flow in the previous section.

We next investigate the effect of  $\Delta t$  on the stability and accuracy of the simulations. Thanks to the discrete energy stability property (Theorem 2.1), fairly large time step sizes can be employed in actual simulations with the current method. Table 7 lists the mean and rms forces on the walls obtained using time step sizes ranging from  $\Delta t = 2.5e - 4$  to  $\Delta t = 1.0$  in the simulations of the hemisphere flow. A fixed  $C_0 = 1000$  and an element order 6 are employed, and the  $\mathbf{u}_0$  field is updated every 20 time steps. We observe that the current method can produce stable simulation results with various  $\Delta t$ , ranging from small to very large values, at lower Reynolds numbers; see the case  $\nu = 0.02$  in Table 7. At higher Reynolds numbers, we observe that the method produces stable results with small to fairly large  $\Delta t$  values. However, when  $\Delta t$  becomes very large the method seems less robust, in that the BiCGStab linear solver may fail to converge

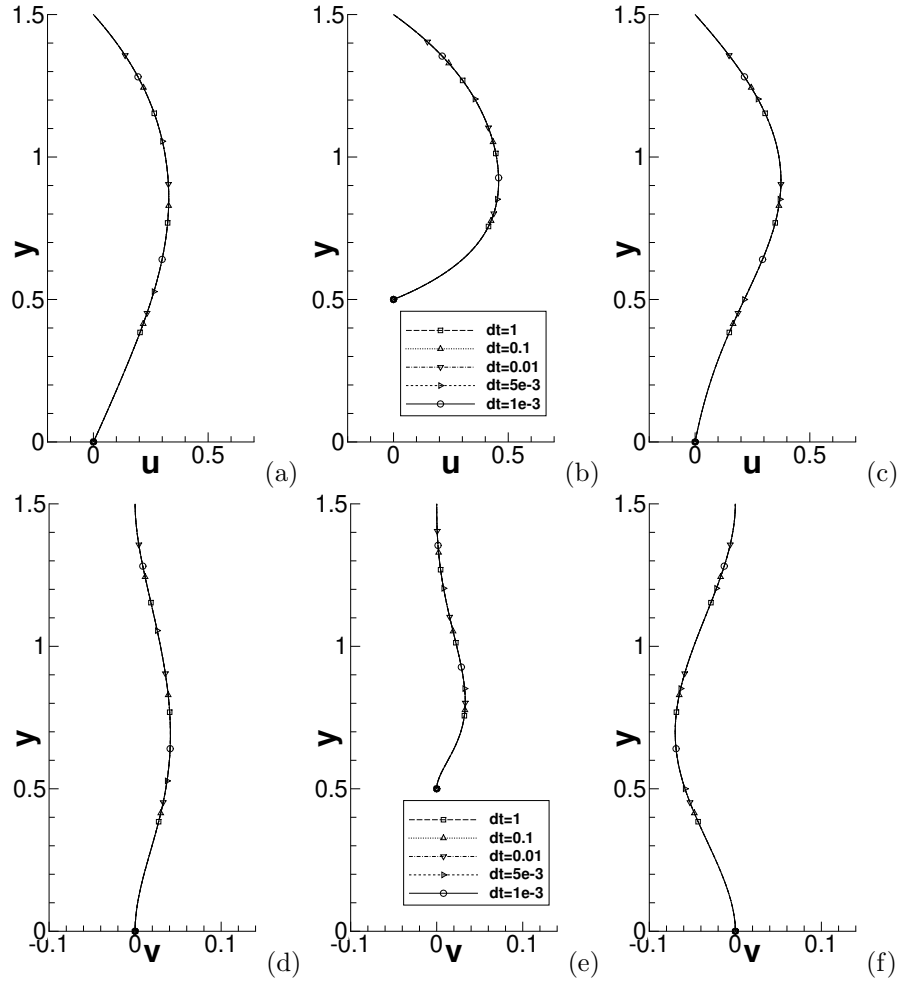


Figure 9: Flow past a hemisphere ( $\nu = 0.02$ ): Comparison of profiles of the streamwise velocity (top row) and vertical velocity (bottom row) at locations (a,d)  $x/d = -1$ , (b,e)  $x/d = 0$ , and (c,f)  $x/d = 1$  computed using the current method with different time step sizes.

for solving the linear algebraic system of equations. For example, for Reynolds numbers corresponding to  $\nu = 0.001$  and  $\nu = 0.0002$ , with  $\Delta t = 0.1$  and larger we observe that the BiCGStab linear solver fails to converge after some time into the computation using the current method. Because the current method involves a non-symmetric velocity coefficient matrix due to the  $\mathbf{M}(\mathbf{u})$  term, with large  $\Delta t$  the conditioning of the velocity linear algebraic system can possibly become poor, which can cause difficulty to the BiCGStab solver. It should be noted that these large  $\Delta t$  values, with which BiCGStab solver encounters a difficulty here, are considerably larger than those maximum  $\Delta t$  values a typical semi-implicit scheme can use in order to maintain stability. For instance, for the hemisphere flow with  $\nu = 0.0002$ , using the semi-implicit scheme from [11] (which also employs a pressure correction-type strategy), the simulation is only stable with  $\Delta t = 2.5e - 4$  or smaller under the same mesh resolution.

Figure 9 shows a comparison of profiles of the steady-state streamwise and vertical velocities across the channel at three downstream locations ( $x/d = 0, \pm 1.0$ ) for  $\nu = 0.02$ . These profiles are computed using the current method with several time step sizes ranging from  $\Delta t = 0.001$  to  $\Delta t = 1.0$ . In these simulations  $C_0 = 1000$ , the element order is 6, and the field  $\mathbf{u}_0$  is updated every 20 time steps. The velocity profiles obtained with different  $\Delta t$ , ranging from small to large values, exactly overlap with one another. This suggests that the current method can produce accurate results with large  $\Delta t$  for this problem.

With the current method the field  $\mathbf{u}_0$ , and hence the velocity coefficient matrix (see equation (13)), is updated every  $k_0$  time steps. We observe that the frequency for  $\mathbf{u}_0$  update can have an influence on the

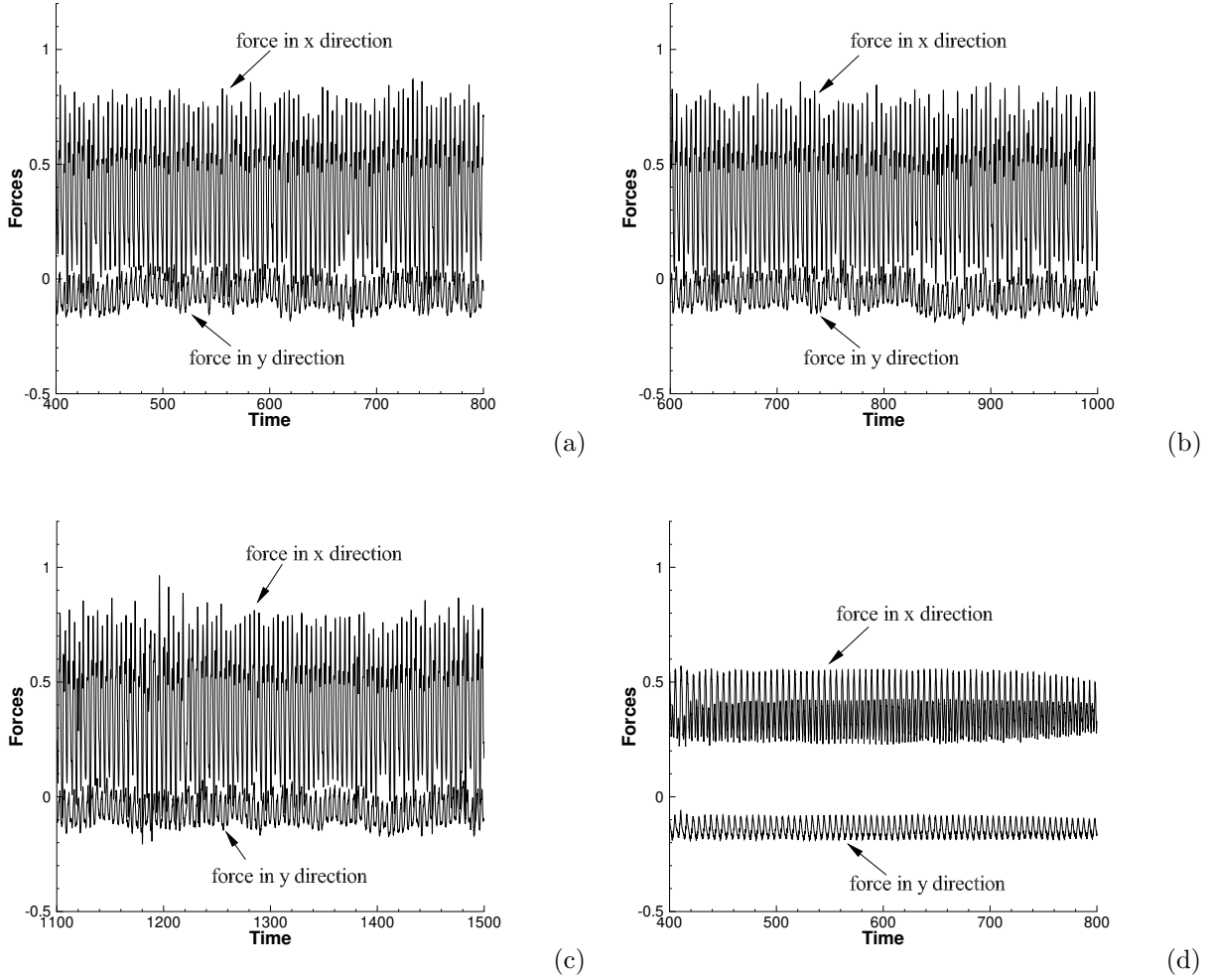


Figure 10: Flow past a hemisphere ( $\nu = 0.001$ ): time histories of the forces on channel walls obtained with different frequency parameter  $k_0$  for updating the field  $\mathbf{u}_0$ . (a)  $k_0 = 20$ , (b)  $k_0 = 100$ , (c)  $k_0 = 200$ , (d)  $k_0 = 500$ .

accuracy of simulation results. With too large a  $k_0$  value, the simulation can lose accuracy. This point is demonstrated by Figure 10, which shows time histories of the forces on walls at  $\nu = 0.001$  with  $\mathbf{u}_0$  updated with different frequencies, ranging from  $k_0 = 20$  to  $k_0 = 500$ . In this set of simulations we have employed  $\Delta t = 0.001$ , element order 6 and  $C_0 = 1000$ . It can be observed that the computed forces have essentially the same characteristics when  $\mathbf{u}_0$  is updated every 20, 100, or 200 time steps. When  $k_0$  increases to 500, however, the computed forces are notably different in terms of the amplitude, frequency and the overall characteristics. This indicates that the accuracy starts to deteriorate.

Table 8 provides the mean and rms forces on the walls at three Reynolds numbers corresponding to  $\nu = 0.02$ , 0.001 and 0.0002 obtained with various  $k_0$  (ranging from 10 to 1000) for updating the field  $\mathbf{u}_0$ . In these tests  $\Delta t = 0.001$ , the element order is 6, and  $C_0 = 1000$ . These data confirm our observations based on the force histories. At  $\nu = 0.02$  the computed forces are basically identical, irrespective of whether  $\mathbf{u}_0$  is updated every 10 time steps or every 1000 time steps. At  $\nu = 0.001$  the computed forces are quite close when  $k_0 = 200$  or below. But their values are notably different with  $k_0 = 500$  and larger. At  $\nu = 0.0002$ , the computed forces start to show notable differences when  $k_0$  increases to 50 and larger. These results suggest that, when  $\mathbf{u}_0$  is updated too rarely, the correction term  $[\mathbf{N}(\mathbf{u}) - \mathbf{M}(\mathbf{u})]$  in equation (12) may become more significant and this can cause larger errors in the simulation results. With higher Reynolds numbers the field

$\nu$	$k_0$	$f_x$	$f'_x$	$f_y$	$f'_y$	Driving force
0.02	10	0.393	0	2.56e-4	0	0.393
	20	0.393	0	8.7e-5	0	0.393
	50	0.393	0	2.61e-4	0	0.393
	100	0.393	0	2.60e-4	0	0.393
	200	0.393	0	2.61e-4	0	0.393
	500	0.393	0	2.59e-4	0	0.393
	1000	0.393	0	2.60e-4	0	0.393
0.001	10	0.394	0.238	-0.0668	0.0562	0.393
	20	0.394	0.238	-0.0636	0.0559	0.393
	50	0.394	0.240	-0.0701	0.0567	0.393
	100	0.394	0.237	-0.0670	0.0561	0.393
	200	0.394	0.243	-0.0685	0.0559	0.393
	500	0.377	0.0858	-0.142	0.0300	0.393
	1000	0.382	0.184	-0.105	0.0657	0.393
0.0002	10	0.389	0.807	0.103	0.410	0.393
	20	0.388	0.812	0.102	0.401	0.393
	50	0.390	0.818	0.212	0.547	0.393
	100	0.397	0.772	0.233	0.530	0.393
	200	0.395	0.554	0.182	0.772	0.393
	500	0.398	0.341	-0.110	0.614	0.393
	1000	0.365	0.327	0.0396	0.818	0.393

Table 8: Flow past a hemisphere: Effect of the frequency parameter  $k_0$  for  $\mathbf{u}_0$  update on the computed forces on walls.

$\nu$	$\Delta t$	$f_x$	$f'_x$	$f_y$	$f'_y$	Driving force
0.02	0.001	0.393	0	1.11e-4	0	0.393
	0.005	0.393	0	2.52e-4	0	0.393
	0.01	0.393	0	2.51e-4	0	0.393
	0.1	0.394	1.87e-4	5.03e-4	2.92e-4	0.393
	1.0	0.393	1.77e-3	8.79e-5	8.07e-4	0.393
0.001	5e-4	0.393	0.238	-6.69e-2	0.123	0.393
	0.001	0.400	0.182	-2.94e-2	0.0954	0.393
	0.005	0.395	0.0620	8.28e-3	8.90e-3	0.393
	0.01	0.394	1.17e-4	2.86e-2	1.59e-4	0.393
	0.1	0.393	1.55e-5	6.90e-4	1.03e-3	0.393
	1.0	0.393	3.37e-6	-4.04e-3	1.04e-2	0.393

Table 9: Flow past a hemisphere: Mean and rms forces on the walls attained using the modified scheme (with  $\mathbf{M}(\mathbf{u}) = 0$ ) with different  $\Delta t$  for  $\nu = 0.02$  and  $\nu = 0.001$ .

$\mathbf{u}_0$  should be updated more frequently in order to maintain accuracy in the simulation results.

The modified scheme with  $\mathbf{M}(\mathbf{u}) = 0$  (see Remark 1) has also been used to simulate the hemisphere in channel problem. Figure 11 shows the steady-state streamwise and vertical velocity profiles at three downstream locations for  $\nu = 0.02$  obtained using this modified scheme. These profiles correspond to several time step sizes ranging from  $\Delta t = 0.001$  to  $\Delta t = 1.0$ .  $C_0 = 1000$  and element order 6 are employed in the simulations. This figure can be compared with Figure 9, which is attained using the current method under identical conditions. While the velocity profiles computed using the modified algorithm with  $\Delta t = 0.01$  and smaller all overlap with one another, those obtained with the larger  $\Delta t = 0.1$  and  $\Delta t = 1.0$  exhibit marked differences than with smaller  $\Delta t$  values. This suggests that the velocity distributions obtained with the larger  $\Delta t$  values are no longer accurate using the modified scheme. In contrast, with the current method the velocity profiles computed with the larger  $\Delta t = 0.1$  and  $\Delta t = 1.0$  are identical to those obtained with the smaller  $\Delta t$  values; see Figure 9. It is further noted that all the velocity profiles obtained using the current

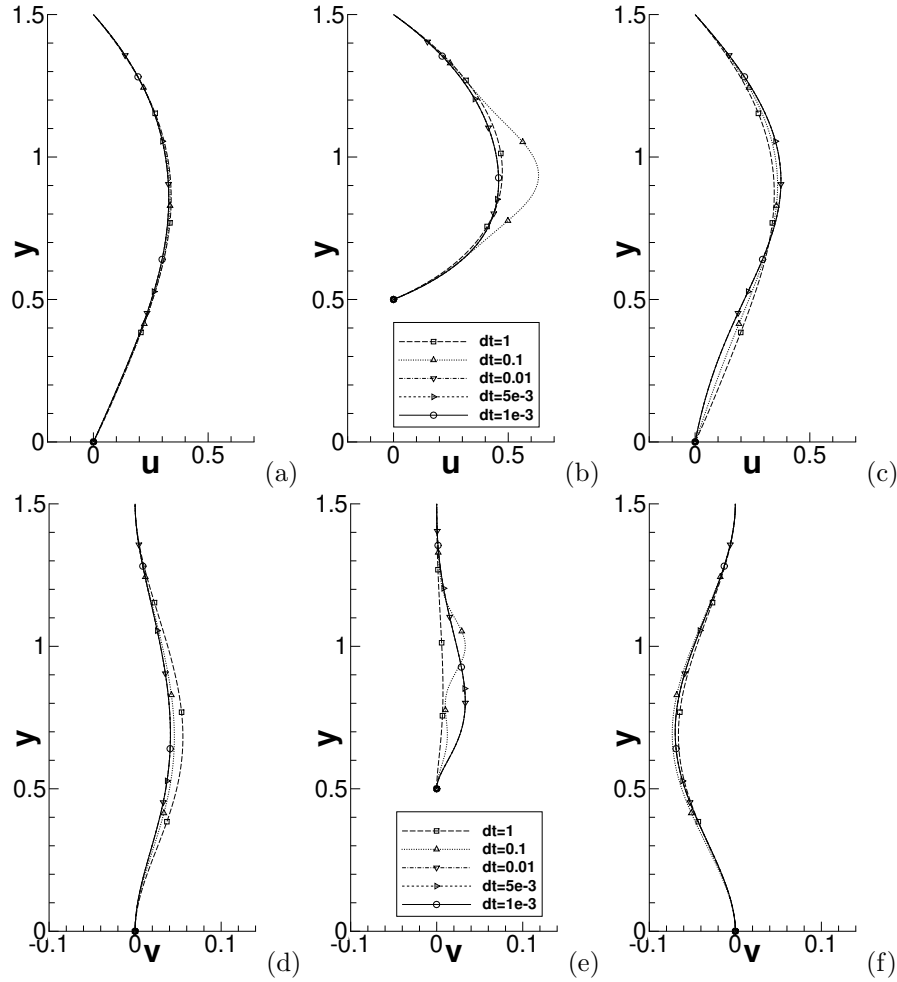


Figure 11: Flow past a hemisphere ( $\nu = 0.02$ ): Comparison of profiles of the streamwise velocity (top row) and vertical velocity (bottom row) at locations (a,d)  $x/d = -1$ , (b,e)  $x/d = 0$ , and (c,f)  $x/d = 1$  obtained using the modified scheme ( $\mathbf{M}(\mathbf{u}) = 0$ ) with different time step sizes.

method in Figure 9 agree with those profiles obtained using the modified scheme with the smaller  $\Delta t$  values. These data suggest that the current method is superior in accuracy to the modified scheme. The current method can produce accurate results at larger time step sizes where the modified algorithm with  $\mathbf{M}(\mathbf{u}) = 0$  ceases to be accurate. This is consistent with the observations with the Kovaszny flow in the previous section.

Table 9 lists the mean and rms forces on the walls computed using the modified scheme ( $\mathbf{M}(\mathbf{u}) = 0$ ) with a number of time step sizes ranging from  $\Delta t = 5.0e - 4$  to  $\Delta t = 1.0$  for  $\nu = 0.02$  and  $\nu = 0.001$ . This table can be compared with Table 7, which is obtained with the current method under identical conditions. We observe that the modified scheme with  $\mathbf{M}(\mathbf{u}) = 0$  is more robust for very large time step sizes. For example, stable simulation results are obtained using the modified scheme with  $\Delta t = 0.1$  and  $\Delta t = 1.0$  for  $\nu = 0.001$ . It is already discussed before that with the current method the BiCGStab linear solver fails to converge for these two cases. Note that in the implementation of the modified scheme with  $\mathbf{M}(\mathbf{u}) = 0$  the conjugate gradient (CG) solver has been used to solve the resultant linear systems, because the coefficient matrix is symmetric positive definite. On the other hand, in the implementation of the current method, the BiCGStab linear solver is used for the velocity linear system and the CG solver is used for the pressure linear system. In terms of accuracy, the data again indicate that the current method is superior for large or fairly large time step sizes. For  $\nu = 0.02$ , the horizontal and vertical forces ( $f_x, f_y$ ) obtained using the modified scheme with  $\Delta t = 0.1$  and  $\Delta t = 1.0$  exhibits slight fluctuations in time, as shown by the non-zero values of

Frequency parameter $k_0$ for $\mathbf{u}_0$ update	average wall-time/step (seconds)
$k_0 = 10$	0.0726
$k_0 = 20$	0.0705
$k_0 = 50$	0.0693
$k_0 = 100$	0.0689
$k_0 = 200$	0.0687
$k_0 = 500$	0.0686
$k_0 = 1000$	0.0685

Table 10: Computational cost of the flow past a hemisphere ( $\nu = 0.001$ ): average wall-time per time step (on two CPU cores) for the current method when the coefficient matrix is updated once every  $k_0$  time steps (element order 6,  $\Delta t = 0.001$ ). With this problem size, it takes 0.109 seconds to compute a time step when the coefficient matrix is updated at that particular step, and it takes 0.0685 seconds to compute a time step when the coefficient matrix is not updated at that step.

the rms forces corresponding to these cases in Table 9. The current method, on the other hand, results in a constant force for these cases. For  $\nu = 0.001$ , the rms forces corresponding to  $\Delta t = 0.001 \sim 0.01$  obtained using the modified scheme exhibit a more pronounced difference when compared with that corresponding to  $\Delta t = 5e - 4$  (see Table 9). With the current method there is essentially no difference or this difference is much smaller (see Table 7).

Let us finally look into the computational cost of the current method. When the field  $\mathbf{u}_0$  is updated at a time step, the coefficient matrix of the linear algebraic system for the velocity needs to be re-computed and re-factorized at that step. This induces an extra cost, which increases with the problem size and can become substantial with a fairly large or large element order. If  $\mathbf{u}_0$  is updated once every  $k_0$  time steps, this extra computational cost is effectively spread over  $k_0$  time steps in the long run. Therefore, the impact induced by the coefficient matrix update can be considerably smaller in terms of the average computational cost per time step. In Table 10 we provide the average wall time per time step (in seconds, using two CPU cores) corresponding to different frequency parameter values ( $k_0$ ) with the current method for the flow past a hemisphere in channel ( $\nu = 0.001$ , element order 6,  $\Delta t = 0.001$ ,  $C_0 = 1000$ ). Note that this is the wall time averaged over a number of time steps. In reality, with this problem size, when  $\mathbf{u}_0$  is updated at a certain time step it takes about 0.109 seconds (on two CPU cores) to compute that step. When  $\mathbf{u}_0$  is not updated at a time step it takes about 0.0685 seconds (on two CPU cores) to compute that step. The wall-time values are collected on a Linux cluster in the authors' institution (Purdue University). These results indicate that with the current method if the field  $\mathbf{u}_0$  is not updated very frequently, the impact of the coefficient-matrix update on the overall computational cost is not significant.

## 4 Concluding Remarks

In the current paper we have developed an energy-stable scheme for simulating the incompressible Navier-Stokes equations. The scheme incorporates a pressure-correction type strategy and the generalized Positive Auxiliary Variable (gPAV) approach. The salient feature of the algorithm lies in that in the gPAV reformulated system the original nonlinear term is replaced by the sum of a linear term ( $\mathbf{M}(\mathbf{u})$ ) and a correction term, and the correction term is put under control by the auxiliary variable. The scheme satisfies a discrete energy stability property, irrespective of the time step sizes. Within each time step, the scheme entails the computation of two copies of the velocity and the pressure, by solving an individual de-coupled linear algebraic system for each of these field variables. The pressure linear system involves a constant and time-independent coefficient matrix, which can be pre-computed. The coefficient matrix for the velocity linear system can be updated periodically, once every  $k_0$  time steps in the current method. If the linear term is set to zero ( $\mathbf{M}(\mathbf{u}) = 0$ ), the velocity coefficient matrix becomes time-independent and can also be pre-computed, which corresponds to the modified scheme suggested in Remark 1. The auxiliary variable, on the other hand, is computed by a well-defined explicit formula, which guarantees the positivity of its computed values. No nonlinear algebraic solver is involved in the current method, for either the field variables or the auxiliary variable.

It is observed that the current method can produce accurate results with large (or fairly large) time step sizes for the incompressible Navier-Stokes equations. The maximum  $\Delta t$  that can lead to accurate simulation results using the current method is typically considerably larger than that with the scheme of [21] or the modified scheme from Remark 1. For example, for the Kovasznay flow (under identical conditions), the current method can still produce accurate results with  $\Delta t = 0.4$ , and the method from [21] can produce accurate results with  $\Delta t \sim 0.009$  (see Table 1 of [21]), while the modified scheme from Remark 1 produces accurate results with only even smaller  $\Delta t$  values. While the current method substantially expands the accuracy range for the time step size, it is noted that when  $\Delta t$  increases to a certain level the method will similarly lose accuracy in the simulation results, even though the computation may be stable. This is similar to those observations in [21, 20].

An apparent downside of the current method is the need for periodic update of the coefficient matrix for the velocity linear algebraic system, which induces an extra cost when compared with the method from [21] and the modified scheme from Remark 1. Since this coefficient matrix is only updated once every  $k_0$  time steps, the extra cost induced by the re-computation of the coefficient matrix is effectively spread over  $k_0$  time steps. In simulations  $k_0$  is typically on the order of several dozen. So the impact of the coefficient-matrix update on the overall cost of the current method is in general quite small, and can be essentially negligible when  $k_0$  is a sizable number.

Another potential drawback of the current method lies in that the coefficient matrix for the velocity linear system is non-symmetric due to the  $\mathbf{M}(\mathbf{u})$  term (but it is positive definite). In the current implementation we have employed the BiCGStab solver when solving the velocity linear algebraic system. In numerical simulations we observe that when the Reynolds number becomes large and with very large  $\Delta t$  this solver can at times encounter difficulties for convergence (see Section 3.3), thus making the method less robust in these cases. On the other hand, the modified scheme from Remark 1 involves coefficient matrices that are symmetric positive definite, and the linear systems are solved using the conjugate gradient (CG) solver in the current implementation. In numerical experiments we observe that this method is very robust with very large  $\Delta t$  values at high Reynolds numbers. It should be noted that, at those  $\Delta t$  values when the BiCGStab solver starts to encounter difficulty, the simulation results are already no longer accurate.

## Appendix A. Approximation for the First Time Step

We summarize the approximation of the flow variables for the first time step in this Appendix. The scheme below ensures that the computed values for  $R^{n+1}|_{n=0}$ ,  $R^{n+1/2}|_{n=0}$  and  $R^{n+3/2}|_{n=0}$  are all positive. The notation here follows that in the main text.

Given  $(\tilde{\mathbf{u}}^0, \mathbf{u}^0, R^0, p^0)$ , we compute the first time step in two substeps. In the first substep we compute an approximation of  $(\tilde{\mathbf{u}}^1, \mathbf{u}^1, R^1, p^1)$ , denoted by  $(\tilde{\mathbf{u}}_a^1, \mathbf{u}_a^1, R_a^1, p_a^1)$ . In the second substep we compute the final  $(\tilde{\mathbf{u}}^1, \mathbf{u}^1, R^1, p^1)$ . These computations are as follows.

First Substep:

For  $\tilde{\mathbf{u}}_a^1$ :

$$\frac{\tilde{\mathbf{u}}_a^1 - \mathbf{u}^0}{\Delta t} + \mathbf{M}(\tilde{\mathbf{u}}_a^1) + \nabla p^0 - \nu \nabla^2 \tilde{\mathbf{u}}_a^1 + \xi_a [\mathbf{N}(\tilde{\mathbf{u}}^0) - \mathbf{M}(\tilde{\mathbf{u}}^0)] = \mathbf{f}^1; \quad (55a)$$

$$\xi_a = \frac{(R_a^1)^2}{E[\tilde{\mathbf{u}}_a^1]}; \quad (55b)$$

$$E[\tilde{\mathbf{u}}_a^1] = \int_{\Omega} \frac{1}{2} |\tilde{\mathbf{u}}_a^1|^2 d\Omega + C_0; \quad (55c)$$

$$\tilde{\mathbf{u}}_a^1 = \mathbf{w}^1, \quad \text{on } \partial\Omega; \quad (55d)$$

For  $\phi_a^1$ :

$$\phi_a^1 = \nabla \cdot \tilde{\mathbf{u}}_a^1; \quad (56)$$

For  $p_a^1$  and  $\mathbf{u}_a^1$ :

$$\frac{\mathbf{u}_a^1 - \tilde{\mathbf{u}}_a^1}{\Delta t} + \nabla (p_a^1 - p^0 + \nu\phi_a^1) = 0; \quad (57a)$$

$$\nabla \cdot \mathbf{u}_a^1 = 0; \quad (57b)$$

$$\mathbf{n} \cdot \mathbf{u}_a^1 = \mathbf{n} \cdot \mathbf{w}^1, \quad \text{on } \partial\Omega; \quad (57c)$$

$$\int_{\Omega} p_a^1 d\Omega = 0; \quad (57d)$$

For  $R_a^{n+1}$ :

$$\begin{aligned} (R_a^1 + R^0) \frac{R_a^1 - R^0}{\Delta t} &= \int_{\Omega} \tilde{\mathbf{u}}_a^1 \cdot \frac{\mathbf{u}_a^1 - \mathbf{u}^0}{\Delta t} \\ &+ \xi_a \left[ -\nu \int_{\Omega} \|\nabla \tilde{\mathbf{u}}_a^1\|^2 d\Omega + \int_{\Omega} \mathbf{f}^1 \cdot \tilde{\mathbf{u}}_a^1 d\Omega + \int_{\Omega} \left( -\bar{P}_a^1 \mathbf{n} + \nu \mathbf{n} \cdot \nabla \tilde{\mathbf{u}}_a^1 - \frac{1}{2} (\mathbf{n} \cdot \mathbf{w}^1) \mathbf{w}^1 \right) \cdot \mathbf{w}^1 d\Omega \right] \\ &- \int_{\Omega} [-\mathbf{M}(\tilde{\mathbf{u}}_a^1) - \nabla P_a^1 + \nu \nabla^2 \tilde{\mathbf{u}}_a^1 - \xi_a (\mathbf{N}(\tilde{\mathbf{u}}^0) - \mathbf{M}(\tilde{\mathbf{u}}^0)) + \mathbf{f}^1] \cdot \tilde{\mathbf{u}}^{n+1} d\Omega \\ &+ (1 - \xi_a) \left[ \left| \int_{\Omega} \mathbf{f}^1 \cdot \tilde{\mathbf{u}}_a^1 d\Omega \right| + \left| \int_{\Omega} \left( -\bar{P}_a^1 \mathbf{n} + \nu \mathbf{n} \cdot \nabla \tilde{\mathbf{u}}_a^1 - \frac{1}{2} (\mathbf{n} \cdot \mathbf{w}^1) \mathbf{w}^1 \right) \cdot \mathbf{w}^1 d\Omega \right| \right]. \end{aligned} \quad (58)$$

Second Substep:

For  $\tilde{\mathbf{u}}^1$ :

$$\frac{\tilde{\mathbf{u}}^1 - \mathbf{u}^0}{\Delta t} + \mathbf{M}(\tilde{\mathbf{u}}^1) + \nabla p^0 - \nu \nabla^2 \tilde{\mathbf{u}}^1 + \xi [\mathbf{N}(\tilde{\mathbf{u}}^0) - \mathbf{M}(\tilde{\mathbf{u}}^0)] = \mathbf{f}^1; \quad (59a)$$

$$\xi = \frac{(R^{3/2})^2}{E[\bar{\mathbf{u}}^{3/2}]}; \quad (59b)$$

$$E[\bar{\mathbf{u}}^{3/2}] = \int_{\Omega} \frac{1}{2} |\bar{\mathbf{u}}^{3/2}|^2 d\Omega + C_0; \quad (59c)$$

$$\tilde{\mathbf{u}}^1 = \mathbf{w}^1, \quad \text{on } \partial\Omega; \quad (59d)$$

For  $\phi^1$ :

$$\phi^1 = \nabla \cdot \tilde{\mathbf{u}}^1; \quad (60)$$

For  $p^1$  and  $\mathbf{u}^1$ :

$$\frac{\mathbf{u}^1 - \tilde{\mathbf{u}}^1}{\Delta t} + \nabla (p^1 - p^0 + \nu\phi^1) = 0; \quad (61a)$$

$$\nabla \cdot \mathbf{u}^1 = 0; \quad (61b)$$

$$\mathbf{n} \cdot \mathbf{u}^1 = \mathbf{n} \cdot \mathbf{w}^1, \quad \text{on } \partial\Omega; \quad (61c)$$

$$\int_{\Omega} p^1 d\Omega = 0; \quad (61d)$$

For  $R^{n+1}$ :

$$\begin{aligned} (R^{3/2} + R^{1/2}) \frac{R^{3/2} - R^{1/2}}{\Delta t} &= \int_{\Omega} \tilde{\mathbf{u}}^1 \cdot \frac{\mathbf{u}^1 - \mathbf{u}^0}{\Delta t} \\ &+ \xi \left[ -\nu \int_{\Omega} \|\nabla \tilde{\mathbf{u}}^1\|^2 d\Omega + \int_{\Omega} \mathbf{f}^1 \cdot \tilde{\mathbf{u}}^1 d\Omega + \int_{\Omega} \left( -\bar{P}^1 \mathbf{n} + \nu \mathbf{n} \cdot \nabla \tilde{\mathbf{u}}^1 - \frac{1}{2} (\mathbf{n} \cdot \mathbf{w}^1) \mathbf{w}^1 \right) \cdot \mathbf{w}^1 d\Omega \right] \\ &- \int_{\Omega} [-\mathbf{M}(\tilde{\mathbf{u}}^1) - \nabla P^1 + \nu \nabla^2 \tilde{\mathbf{u}}^1 - \xi (\mathbf{N}(\tilde{\mathbf{u}}^0) - \mathbf{M}(\tilde{\mathbf{u}}^0)) + \mathbf{f}^1] \cdot \tilde{\mathbf{u}}^{n+1} d\Omega \\ &+ (1 - \xi) \left[ \left| \int_{\Omega} \mathbf{f}^1 \cdot \tilde{\mathbf{u}}^1 d\Omega \right| + \left| \int_{\Omega} \left( -\bar{P}^1 \mathbf{n} + \nu \mathbf{n} \cdot \nabla \tilde{\mathbf{u}}^1 - \frac{1}{2} (\mathbf{n} \cdot \mathbf{w}^1) \mathbf{w}^1 \right) \cdot \mathbf{w}^1 d\Omega \right| \right]. \end{aligned} \quad (62)$$

The symbols involved in the above equations are explained as follows. In equations (55b) and (58)  $\bar{\mathbf{u}}_a^1$  is an approximation of  $\mathbf{u}_a^1$  and will be specified later in (79).  $P_a^1$  and  $\bar{P}_a^1$  are given by

$$P_a^1 = p_a^1 + \nu\phi_a^1, \quad \bar{P}_a^1 = \bar{p}_a^1 + \nu\bar{\phi}_a^1, \quad (63)$$

where  $\bar{p}_a^1$  and  $\bar{\phi}_a^1$  are approximations of  $p_a^1$  and  $\phi_a^1$  to be specified later in (79). In equations (59b) and (62)  $\bar{\mathbf{u}}^{3/2}$ ,  $R^{3/2}$  and  $R^{1/2}$  are given by,

$$\begin{cases} \bar{\mathbf{u}}^{3/2} = \frac{3}{2}\mathbf{u}_a^1 - \frac{1}{2}\mathbf{u}^0, \\ R^{3/2} = \frac{3}{2}R^1 - \frac{1}{2}R^0, \\ R^{1/2} = \frac{1}{2}(R_a^1 + R^0). \end{cases} \quad (64)$$

$P^1$  and  $\bar{P}^1$  are given by

$$P^1 = p^1 + \nu\phi^1, \quad \bar{P}^1 = \bar{p}^1 + \nu\bar{\phi}^1, \quad (65)$$

where  $\bar{p}^1$  and  $\bar{\phi}^1$  are approximations of  $p^1$  and  $\phi^1$  to be specified later in (79).

A combination of equations (55a), (57a) and (58) leads to

$$\frac{(R_a^1)^2 - (R^0)^2}{\Delta t} = \xi_a \left[ -\nu \int_{\Omega} \|\nabla \bar{\mathbf{u}}_a^1\|^2 d\Omega + B_1 + B_2 \right] + (1 - \xi_a) (|B_1| + |B_2|), \quad (66)$$

where

$$B_1 = \int_{\Omega} \mathbf{f} \cdot \bar{\mathbf{u}}_a^1 d\Omega, \quad B_2 = \int_{\Omega} \left( -\bar{P}_a^1 \mathbf{n} + \nu \mathbf{n} \cdot \nabla \bar{\mathbf{u}}_a^1 - \frac{1}{2}(\mathbf{n} \cdot \mathbf{w}^1) \mathbf{w}^1 \right) \cdot \mathbf{w}^1 d\Omega. \quad (67)$$

In light of (55b) we then have

$$\begin{cases} \xi_a = \frac{(R^0)^2 + (|B_1| + |B_2|)\Delta t}{E[\bar{\mathbf{u}}_a^1] + \left[ \nu \int_{\Omega} \|\nabla \bar{\mathbf{u}}_a^1\|^2 d\Omega + (|B_1| - B_1) + (|B_2| - B_2) \right] \Delta t}, \\ R_a^1 = \sqrt{\xi_a E[\bar{\mathbf{u}}_a^1]}. \end{cases} \quad (68)$$

Since  $R^0 > 0$  according to (17), we conclude that  $\xi_a > 0$  and  $R_a^1 > 0$  from the above equations. Then based on equation (64) we conclude that  $R^{1/2} > 0$ .

A combination of equations (59a), (61a) and (62) leads to

$$\frac{(R^{3/2})^2 - (R^{1/2})^2}{\Delta t} = \xi \left[ -\nu \int_{\Omega} \|\nabla \bar{\mathbf{u}}^1\|^2 d\Omega + D_1 + D_2 \right] + (1 - \xi) (|D_1| + |D_2|), \quad (69)$$

where

$$D_1 = \int_{\Omega} \mathbf{f} \cdot \bar{\mathbf{u}}^1 d\Omega, \quad D_2 = \int_{\Omega} \left( -\bar{P}^1 \mathbf{n} + \nu \mathbf{n} \cdot \nabla \bar{\mathbf{u}}^1 - \frac{1}{2}(\mathbf{n} \cdot \mathbf{w}^1) \mathbf{w}^1 \right) \cdot \mathbf{w}^1 d\Omega. \quad (70)$$

Note that  $R^{3/2}$  and  $R^{1/2}$  are defined by (64). In light of (59b) we then have

$$\begin{cases} \xi = \frac{(R^{1/2})^2 + (|D_1| + |D_2|)\Delta t}{E[\bar{\mathbf{u}}^{3/2}] + \left[ \nu \int_{\Omega} \|\nabla \bar{\mathbf{u}}^1\|^2 d\Omega + (|D_1| - D_1) + (|D_2| - D_2) \right] \Delta t}, \\ R^{3/2} = \sqrt{\xi E[\bar{\mathbf{u}}^{3/2}]}, \\ R^1 = \frac{2}{3}R^{3/2} + \frac{1}{3}R^0. \end{cases} \quad (71)$$

Since  $R^{1/2} > 0$ , we conclude that  $\xi > 0$ ,  $R^{3/2} > 0$  and  $R^1 > 0$ .

In the above formulas  $(\tilde{\mathbf{u}}_a^1, \mathbf{u}_a^1, p_a^1, \phi_a^1)$  and  $(\tilde{\mathbf{u}}^1, \mathbf{u}^1, p^1, \phi^1)$  still need to be determined, and the variables with overbars need to be specified. We compute these variables as follows. First define two sets of field variables  $(\tilde{\mathbf{u}}_1^1, \mathbf{u}_1^1, p_1^1, \phi_1^1)$  and  $(\tilde{\mathbf{u}}_2^1, \mathbf{u}_2^1, p_2^1, \phi_2^1)$  as solutions to the following equations:

For  $(\tilde{\mathbf{u}}_1^1, \mathbf{u}_1^1, p_1^1, \phi_1^1)$ :

$$\begin{cases} \frac{\tilde{\mathbf{u}}_1^1}{\Delta t} + \mathbf{M}(\tilde{\mathbf{u}}_1^1) - \nu \nabla^2 \tilde{\mathbf{u}}_1^1 = \mathbf{f}^1 + \frac{\mathbf{u}^0}{\Delta t} - \nabla p^0; \\ \tilde{\mathbf{u}}_1^1 = \mathbf{w}^1, \quad \text{on } \partial\Omega; \end{cases} \quad (72)$$

$$\phi_1^1 = \nabla \cdot \tilde{\mathbf{u}}_1^1; \quad (73)$$

$$\begin{cases} \frac{\mathbf{u}_1^1}{\Delta t} + \nabla p_1^1 = \frac{\tilde{\mathbf{u}}_1^1}{\Delta t} - \nabla(-p^0 + \nu \phi_1^1); \\ \nabla \cdot \mathbf{u}_1^1 = 0; \\ \mathbf{n} \cdot \mathbf{u}_1^1 = \mathbf{n} \cdot \mathbf{w}^1, \quad \text{on } \partial\Omega; \\ \int_{\Omega} p_1^1 d\Omega = 0. \end{cases} \quad (74)$$

For  $(\tilde{\mathbf{u}}_2^1, \mathbf{u}_2^1, p_2^1, \phi_2^1)$ :

$$\begin{cases} \frac{\tilde{\mathbf{u}}_2^1}{\Delta t} + \mathbf{M}(\tilde{\mathbf{u}}_2^1) - \nu \nabla^2 \tilde{\mathbf{u}}_2^1 = \mathbf{N}(\tilde{\mathbf{u}}^0) - \mathbf{M}(\tilde{\mathbf{u}}^0) \\ \tilde{\mathbf{u}}_2^1 = 0, \quad \text{on } \partial\Omega; \end{cases} \quad (75)$$

$$\phi_2^1 = \nabla \cdot \tilde{\mathbf{u}}_2^1; \quad (76)$$

$$\begin{cases} \frac{\mathbf{u}_2^1}{\Delta t} + \nabla p_2^1 = \frac{\tilde{\mathbf{u}}_2^1}{\Delta t} - \nu \phi_2^1; \\ \nabla \cdot \mathbf{u}_2^1 = 0; \\ \mathbf{n} \cdot \mathbf{u}_2^1 = 0, \quad \text{on } \partial\Omega; \\ \int_{\Omega} p_2^1 d\Omega = 0. \end{cases} \quad (77)$$

It is then straightforward to verify that the solutions to equations (55a)–(58) and (59a)–(62) are, for given  $\xi_a$  and  $\xi$ ,

$$\begin{cases} \tilde{\mathbf{u}}_a^1 = \tilde{\mathbf{u}}_1^1 + \xi_a \tilde{\mathbf{u}}_2^1, \\ \mathbf{u}_a^1 = \mathbf{u}_1^1 + \xi_a \mathbf{u}_2^1, \\ \phi_a^1 = \phi_1^1 + \xi_a \phi_2^1, \\ p_a^1 = p_1^1 + \xi_a p_2^1; \end{cases} \quad \begin{cases} \tilde{\mathbf{u}}^1 = \tilde{\mathbf{u}}_1^1 + \xi \tilde{\mathbf{u}}_2^1, \\ \mathbf{u}^1 = \mathbf{u}_1^1 + \xi \mathbf{u}_2^1, \\ \phi^1 = \phi_1^1 + \xi \phi_2^1, \\ p^1 = p_1^1 + \xi p_2^1. \end{cases} \quad (78)$$

We specify the barred variables as follows,

$$\begin{cases} \bar{\mathbf{u}}_a^1 = \bar{\mathbf{u}}^1 = \tilde{\mathbf{u}}_1^1 + \tilde{\mathbf{u}}_2^1, \\ \bar{\phi}_a^1 = \bar{\phi}^1 = \phi_1^1 + \phi_2^1, \\ \bar{p}_a^1 = \bar{p}^1 = p_1^1 + p_2^1. \end{cases} \quad (79)$$

Note that the field equations (72)–(77) can be solved in a way analogous to the discussions in Section 2.3. The details will not be provided here.

Therefore we compute  $(\bar{\mathbf{u}}^1, \mathbf{u}^1, p^1, R^1)$  by the following procedure:

- Solve equations (72)–(74) for  $(\tilde{\mathbf{u}}_1^1, \mathbf{u}_1^1, p_1^1, \phi_1^1)$ ;  
Solve (75)–(77) for  $(\tilde{\mathbf{u}}_2^1, \mathbf{u}_2^1, p_2^1, \phi_2^1)$ ;
- Compute  $(\bar{\mathbf{u}}_a^1, \bar{P}_a^1)$  by equations (79) and (63);  
Compute  $\xi_a$  and  $R_a^1$  by equation (68);  
Compute  $(\bar{\mathbf{u}}_a^1, \mathbf{u}_a^1, p_a^1)$  by equation (78);
- Compute  $(\bar{\mathbf{u}}^1, \bar{P}^1)$  by equations (79) and (65);  
Compute  $\bar{\mathbf{u}}^{3/2}$  and  $R^{1/2}$  by equation (64);  
Compute  $\xi$  and  $R^1$  by equation (71);  
Compute  $(\bar{\mathbf{u}}^1, \mathbf{u}^1, p^1)$  by equation (78).

It is noted that the computed values have the property  $R^1 > 0$ ,  $R^{1/2} > 0$  and  $R^{3/2} > 0$ .

## Acknowledgement

This work was partially supported by NSF (DMS-1522537).

## References

- [1] H.M. Blackburn and R.D. Henderson. A study of two-dimensional flow past an oscillating cylinder. *Journal of Fluid Mechanics*, 385:255–286, 1999.
- [2] H.M. Blackburn and S.J. Sherwin. Formulation of a Galerkin spectral element-fourier method for three-dimensional incompressible flows in cylindrical geometries. *Journal of Computational Physics*, 197:759–778, 2004.
- [3] D.L. Brown, R. Cortez, and M.L. Minion. Accurate projection methods for the incompressible Navier-Stokes equations. *J. Comput. Phys.*, 168:464–499, 2001.
- [4] H. Chen, S. Sun, and T. Zhang. Energy stability analysis of some fully discrete numerical schemes for incompressible navier-stokes equations on staggered grids. *Journal of Scientific Computing*, 75:427–456, 2018.
- [5] L. Chen, J. Shen, and C.J. Xu. A unstructured nodal spectral-element method for the navier-stokes equations. *Communications in Computational Physics*, 12:315–336, 2012.
- [6] A.J. Chorin. Numerical solution of the Navier-Stokes equations. *Math. Comput.*, 22:745–762, 1968.
- [7] S. Dong. An outflow boundary condition and algorithm for incompressible two-phase flows with phase field approach. *Journal of Computational Physics*, 266:47–73, 2014.
- [8] S. Dong. A convective-like energy-stable open boundary condition for simulations of incompressible flows. *Journal of Computational Physics*, 302:300–328, 2015.
- [9] S. Dong, G.E. Karniadakis, and C. Chrysosostomidis. A robust and accurate outflow boundary condition for incompressible flow simulations on severely-truncated unbounded domains. *Journal of Computational Physics*, 261:83–105, 2014.
- [10] S. Dong and J. Shen. An unconditionally stable rotational velocity-correction scheme for incompressible flows. *Journal of Computational Physics*, 229:7013–7029, 2010.
- [11] S. Dong and J. Shen. A pressure correction scheme for generalized form of energy-stable open boundary conditions for incompressible flows. *Journal of Computational Physics*, 291:254–278, 2015.
- [12] J.L. Guermond, P. Mineev, and J. Shen. Error analysis of pressure-correction schemes for the time-dependent stokes equations with open boundary conditions. *SIAM J. Numer. Anal.*, 43:239–258, 2005.

- [13] B. Hyungso and G.E. Karniadakis. Subiteration leads to accuracy and stability enhancements of semi-implicit schemes for the navier-stokes equations. *Journal of Computational Physics*, 230:4384–4402, 2011.
- [14] N. Jiang, M. Mohebujjaman, L.G. Rebholz, and C. Trenchea. An optimally accurate discrete regularization for second order timestepping methods for navier-stokes equations. *Comput. Methods Appl. Mech. Engrg.*, 310:388–405, 2016.
- [15] G.E. Karniadakis, M. Israeli, and S.A. Orszag. High-order splitting methods for the incompressible Navier-Stokes equations. *J. Comput. Phys.*, 97:414–443, 1991.
- [16] G.E. Karniadakis and S.J. Sherwin. *Spectral/hp element methods for computational fluid dynamics, 2nd edn.* Oxford University Press, 2005.
- [17] J. Kim and P. Moin. Application of a fractional-step method to incompressible Navier-Stokes equations. *J. Comput. Phys.*, 59:308–323, 1985.
- [18] L.I.G. Kovaszny. Laminar flow behind a two-dimensional grid. *Proc. Cambridge Phil. Soc.*, 44:58, 1948.
- [19] A. Labovsky, W.J. Layton, C.C. Manica, M. Neda, and L.G. Rebholz. The stabilized extrapolated trapezoidal finite-element method for the Navier-Stokes equations. *Comput. Methods Appl. Mech. Engrg.*, 198:958–974, 2009.
- [20] L. Lin, X. Liu, and S. Dong. A gPAV-based unconditionally energy-stable scheme for incompressible flows with outflow/open boundaries. *arXiv:1908.01852*, 2019.
- [21] L. Lin, Z. Yang, and S. Dong. Numerical approximation of incompressible Navier-Stokes equations based on an auxiliary energy variable. *Journal of Computational Physics*, 388:1–22, 2019.
- [22] J.-G. Liu, J. Liu, and R.L. Pego. Stability and convergence of efficient Navier-Stokes solvers via a commutator estimate. *Comm. Pure Appl. Math.*, LX:1443–1487, 2007.
- [23] B. Sanderse. Energy-conserving runge-kutta methods for the incompressible navier-stokes equations. *J. Comput. Phys.*, 233:100–131, 2013.
- [24] D. Serson, J.R. Meneghini, and S.J. Sherwin. Velocity-correction schemes for the incompressible navier-stokes equations in general coordinate systems. *Journal of Computational Physics*, 316:243–254, 2016.
- [25] J. Shen. On error estimate of projection methods for Navier-Stokes equations: first-order schemes. *SIAM J. Numer. Anal.*, 29:57–77, 1992.
- [26] J. Shen, J. Xu, and J. Yang. The scalar auxiliary variable (sav) approach for gradient flows. *Journal of Computational Physics*, 353:407–416, 2018.
- [27] S.J. Sherwin and G.E. Karniadakis. A triangular spectral element method: applications to the incompressible navier-stokes equations. *Comput. Meth. Appl. Mech. Engrg.*, 123:189–229, 1995.
- [28] J.C. Simo and F. Armero. Unconditional stability and long-term behavior of transient algorithms for the incompressible Navier-Stokes and Euler equations. *Comput. Methods Appl. Mech. Engrg.*, 111:111–154, 1994.
- [29] R. Temam. Sur l’approximation de la solution des equations de Navier-Stokes par la methods des pas fractionnaires ii. *Arch. Ration. Mech. Anal.*, 33:377–385, 1969.
- [30] R.W.C.P. Verstappen and A.E.P. Veldman. Symmetry-preserving discretization of turbulent flow. *Journal of Computational Physics*, 187:343–368, 2003.
- [31] C.J. Xu and R. Pasquetti. On the efficiency of semi-implicit and semi-lagrangeian spectral methods for the calculation of incompressible flows. *International Journal for Numerical Methods in Fluids*, 35:319–340, 2001.

- [32] X. Yang. Linear, first and second-order, unconditionally energy stable numerical schemes for the phase field model of homopolymer blends. *Journal of Computational Physics*, 327:294–316, 2016.
- [33] Z. Yang and S. Dong. A roadmap for discretely energy-stable schemes for dissipative systems based on a generalized auxiliary variable with guaranteed positivity. arXiv:1904.00141.
- [34] Z. Yang and S. Dong. An unconditionally energy-stable scheme based on an implicit auxiliary energy variable for incompressible two-phase flows with different densities involving only precomputable coefficient matrices. *Journal of Computational Physics*, 393:229–257, 2019.
- [35] Z. Yang, L. Lin, and S. Dong. A family of second-order energy-stable schemes for Cahn-Hilliard type equations. *Journal of Computational Physics*, 383:24–54, 2019.